ACS APPLIED MATERIALS & INTERFACES

www.acsami.org

Research Article

3D Hierarchical $Ti_3C_2T_X$@PANI-Reduced Graphene Oxide Heterostructure Hydrogel Anode and Defective Reduced Graphene Oxide Hydrogel Cathode for High-Performance Zinc Ion Capacitors

Peng Liao, Zenghui Qiu,* Xin Zhang, Wenjie Yan, Haijun Xu,* Colton Jones, and Shaowei Chen*

Cite This: *ACS Appl. Mater. Interfaces* 2023, 15, 48416−48430

Read Online

ACCESS | Metrics & More | Article Recommendations

ABSTRACT: The practical application of supercapacitors (SCs) has been known to be restricted by low energy density, and zinc ion capacitors (ZICs) with a capacitive cathode and a battery-type anode have emerged as a unique technology that can effectively mitigate the issue. To this end, the design of electrodes with low electrochemical impedance, high specific capacitance, and outstanding reaction stability represents a critical first step. Herein, we report the synthesis of hierarchical $Ti_3C_2T_X$@PANI heterostructures by uniform deposition of conductive polyaniline (PANI) polymer nanofibers on the exposed surface of the $Ti_3C_2T_X$ nanosheets, which are then assembled into a three-dimensional (3D) cross-linking framework by a graphene oxide (GO)-assisted self-convergence hydrothermal strategy. This resulting 3D $Ti_3C_2T_X$@PANI-reduced graphene oxide ($Ti_3C_2T_X$@PANI-RGO) heterostructure hydrogel shows a large surface area (488.75 F g^{-1} at 0.5 A g^{-1}), outstanding electrical conductivity, and fast reaction kinetics, making it a promising electrode material. Separately, defective RGO (DRGO) hydrogels are prepared by a patterning process, and they exhibit a broad and uniform distribution of mesopores, which is conducive to ion transport with an excellent specific capacitance (223.52 F g^{-1} at 0.5 A g^{-1}). A ZIC is subsequently constructed by utilizing $Ti_3C_2T_X$@PANI-RGO as the anode and DRGO as the cathode, which displays an extensive operating voltage (0−3.0 V), prominent energy density (1060.96 Wh kg^{-1} at 761.32 W kg^{-1}, 439.87 Wh kg^{-1} at 9786.86 W kg^{-1}), and durable cycle stability (retaining 67.9% of the original capacitance after 4000 cycles at 6 A g^{-1}). This study underscores the immense prospect of the $Ti_3C_2T_X$-based heterostructure hydrogel and DRGO as a feasible anode and cathode for ZICs, respectively.

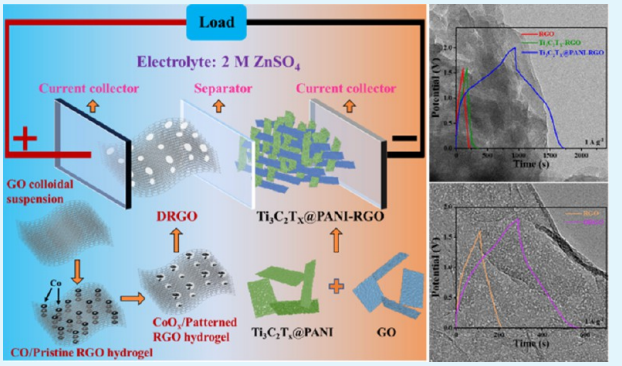

KEYWORDS: *$Ti_3C_2T_X$@PANI heterostructure, intercalation, defective graphene, 3D porous hydrogel, high energy density, zinc ion capacitor*

INTRODUCTION

Supercapacitors (SCs) represent a unique energy storage technology for diverse applications,[1−3] which are divided into 3 categories, double-layer capacitors (EDLCs), pseudocapacitors, and asymmetric supercapacitors (ASCs), on the foundation of the energy storage principles.[4] EDLCs store charge by electrostatic attraction between positive and negative ions without a Faraday process.[5] Pseudocapacitors store charge through Faraday redox reactions, which are related to valence state changes caused by electron transfer.[6,7] ASCs are SCs with a pseudocapacitive positive electrode and a double-layer capacitive negative electrode.[8] Yet, while SCs possess marked advantages, such as fast charging and discharging rates, good rate capability, and reliable stability, the energy density of SCs has remained limited by the electrolyte ions.[9] ZICs represent a unique architecture which combines a capacitive cathode with an ion battery anode and can significantly enhance the energy density.[10−12]

In electrochemical energy storage systems,[13−15] lithium ion-based devices typically entail a strict battery assembly caused by the use of toxic and flammable organic electrolytes; for sodium ion devices, the performance is known to be hampered by a low operating voltage, large radius of sodium ions, slow reaction kinetics, and poor stability of electrodes,[16] whereas for the potassium ion-based system, the large ionic radius of *K* leads to a serious limitation of ion transport and cycling stability.[17] These issues can be effectively mitigated with ZICs.[11,18]

Received: July 27, 2023
Accepted: September 19, 2023
Published: October 4, 2023

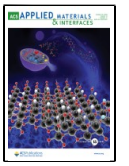

Two-dimensional (2D) nanomaterials have been used comprehensively as SC electrodes on the foundation of a large reaction plane and double-layer capacitance, with pseudocapacitance from the corners.[19,20] MXenes,[3,19] a group of 2D transition metal carbides, nitrides, or carbonitrides (with a formula of $M_{n+1}X_nT_Z$, where M represents a transition metal, X represents C and/or N, n typically ranges from 1 to 3, and T_Z represents the external functional group), are prepared by removing the A atomic thickness of MAX phases.[21,22] Among these, $Ti_3C_2T_X$ has emerged as an effective material for SC electrodes, owing to its high metallic conductivity, excellent hydrophilicity, adjustable layer spacing, and rich redox active sites. Additionally, the abundant surface functional groups/defects and unique 2D hierarchical structure of $Ti_3C_2T_X$ render it possible to construct unique heterostructures, which can not only strengthen the individual properties of each constituent but also exhibit a synergistic effect of excellent structural stability, ultrahigh specific capacitance, and good electrical conductivity.[19,23]

Nevertheless, stacking of the $Ti_3C_2T_X$ layers may occur due to the van der Waals interactions, which can seriously limit the specific surface area and pore distribution and hence the electrochemical performance.[24−26] To mitigate this issue, aniline (ANI) monomers can be chemisorbed onto the surface of the $Ti_3C_2T_X$ nanosheets and polymerized in situ to prepare the $Ti_3C_2T_X$@PANI heterostructure. This effectively increases the interlayer spacing, provides abundant ion/electron transport channels and active sites, and dramatically boosts the electrochemical reaction kinetics.[27,28] Notably, the resultant fiber-shaped polyaniline (PANI) possesses high electric conductivity and large relative molecular mass[29−32] and can store a large amount of charge under an electric field through fast invertible doping and dedoping redox reactions of p-type or n-type elements.[29]

GO is another 2D-layered material[33] and can be used as a cross-linker to prepare $Ti_3C_2T_X$@PANI-RGO heterostructure hydrogels via a low-temperature hydrothermal self-assembly method.[34,35] The 3D porous structure can not only effectively prevent self-restacking but also provide abundant electrochemical active sites and fast ion/electron transport channels to further boost the reaction kinetics.[36] Additionally, the disordered structure formed from the GO-assisted self-convergence hydrothermal procedure can inhibit the structure expansions of MXene-based hydrogels during the repeated charge/discharge process, which can effectively improve the inherent problems of dendrite growth compared with traditional metal zinc anodes, resulting in an excellent electrochemical stability. It is therefore envisioned that $Ti_3C_2T_X$@PANI-RGO hydrogels may be used as high-performance ZIC anodes.[23,37]

The $\pi-\pi$ interactions between the RGO layers are known to result in serious stacking of the nanosheets,[38,39] which can compromise the mesopore distribution, reduce active sites, impede ion transport, and slow reaction kinetics.[40,41] Yet, with a wide distribution of mesoporous defects on the surface of RGO,[42,43] the agglomeration can be effectively mitigated, and active sites can be created providing rich pathways for ion penetration.[44] Defects can be effectively generated by the catalytic gasification of Co particles with C atoms on the surface of RGO, and then the 3D DRGO hydrogel is prepared by acid etching.[45] Compared to traditional carbon-based materials, the 3D DRGO hydrogels possess a large specific surface area and an abounding mesoporous structure and can be used as a promising ZIC cathode.[46,47]

In this study, the 3D-stratified $Ti_3C_2T_X$@PANI-RGO heterostructure hydrogel was synthesized through a convenient and effective strategy and used as an anode for ZICs. The hierarchical $Ti_3C_2T_X$@PANI heterostructure was prepared by chemisorption and polymerization and pieced into highly conductive 3D porous cross-linked hydrogels by a low-temperature hydrothermal GO-assisted self-interacting approach producing hierarchical $Ti_3C_2T_X$@PANI-RGO heterostructure hydrogels. Moreover, DRGO hydrogels were prepared by defect engineering with metal Co cocatalytic gasification and used as the cathode for ZICs. The resulting DRGO//$Ti_3C_2T_X$@PANI-RGO ZIC device possessed a potential window up to 3.0 V (0−3.0 V), a remarkable specific capacitance (848.77 F g^{-1} at 0.5 A g^{-1}), an ultrahigh energy density (1060.96 Wh kg^{-1} at 761.32 W kg^{-1}), and considerable circulation stability (retaining 67.9% of the original capacitance after 4000 periods).

EXPERIMENTAL SECTION

Material Preparation. *$Ti_3C_2T_X$ MXene.* The Ti_3AlC_2 MAX-phase precursor was prepared by ball-milling the Al, C, and TiH_2 mixture at a 3:1.2:2 molar ratio for 24 h using zirconia balls, and the mixture was heated to 1350 °C under an Ar atmosphere for 2 h. Subsequently, the Al layers of the resulting Ti_3AlC_2 powders (<38 μm) were etched to produce $Ti_3C_2T_X$ MXene in the shape of a multilayer accordion. Specifically, 1 g of LiF (99%) was added to 20 mL of 9 M HCl (36%) containing 1 g of Ti_3AlC_2 powder under vigorous stirring in an ice bath for 1 h, followed by stirring at 40 °C for 40 h to etch Ti_3AlC_2. Repeated centrifugation of the $Ti_3C_2T_X$ suspension was carried out with distilled water and anhydrous ethanol at 6000 rpm until the pH became neutral. The well-proportioned $Ti_3C_2T_X$ solution was acquired by sonicating the suspension under an Ar gas stream and centrifuging at 6000 rpm for 2 h. The dark green supernatant was collected and freeze-dried to obtain $Ti_3C_2T_X$.

$Ti_3C_2T_X$@PANI Heterostructure. 0.1 g amount of $Ti_3C_2T_X$ MXene was added into 15 mL of 1 M HCl, and then 0.1 mL of aniline (99.5%) was added under magnetic stirring at 3 °C for 25 min, followed by 10 mL of 1 M HCl and 1.34 g of ammonium persulfate (APS, 98.0%). This solution was stirred magnetically at 3 °C for 8 h. This product was obtained by centrifugation (6000 rpm) for 8 times with distilled water and absolute ethanol. $Ti_3C_2T_X$@PANI heterostructures were obtained by lyophilization for 24 h. PANI was prepared in the same manner but without the addition of $Ti_3C_2T_X$.

3D $Ti_3C_2T_X$@PANI-RGO Heterostructure Hydrogel. GO nanosheets were first prepared from graphite flakes (90%) using a modified Hummer's method.[48] The obtained GO was dispersed in distilled water under sonication for 5 h to prepare a uniform colloidal suspension (2 mg mL^{-1}). Centrifugation was performed at 6000 rpm for 30 min to isolate the thin-layer components. Eight mg of the $Ti_3C_2T_X$@PANI powder was then dispersed in 2 mL of the colloidal suspension of GO under magnetic stirring for 1 h. Subsequently, 8 mg of L-ascorbic acid (mass ratio 1:2 with GO) was added to the mixture under sonication for 1 h. $Ti_3C_2T_X$@PANI-RGO hydrogels were generated after 6 h of hydrothermal treatment at 90 °C. The obtained products were rinsed with distilled water until the pH was about 7. As a control, RGO and $Ti_3C_2T_X$-RGO hydrogels were prepared in the same way.

3D DRGO Hydrogel. A homogeneous GO/Co mixture (mass ratio 9:1) was formed by dispersing 0.2 mg of Co pellets (99.9%) into 0.9 mL of GO (2 mg mL^{-1}) solution under stirring and sonication for 2 h each. RGO/Co hybrid hydrogels were prepared via hydrothermal treatment at 90 °C for 6 h after the addition of L-ascorbic acid (3.6 mg) at a ratio of 1:2, rinsed with distilled water and absolute ethanol, and freeze-dried. The above products were oxidized at 350 °C for 0.5 h,

https://doi.org/10.1021/acsami.3c11035
ACS Appl. Mater. Interfaces 2023, 15, 48416−48430

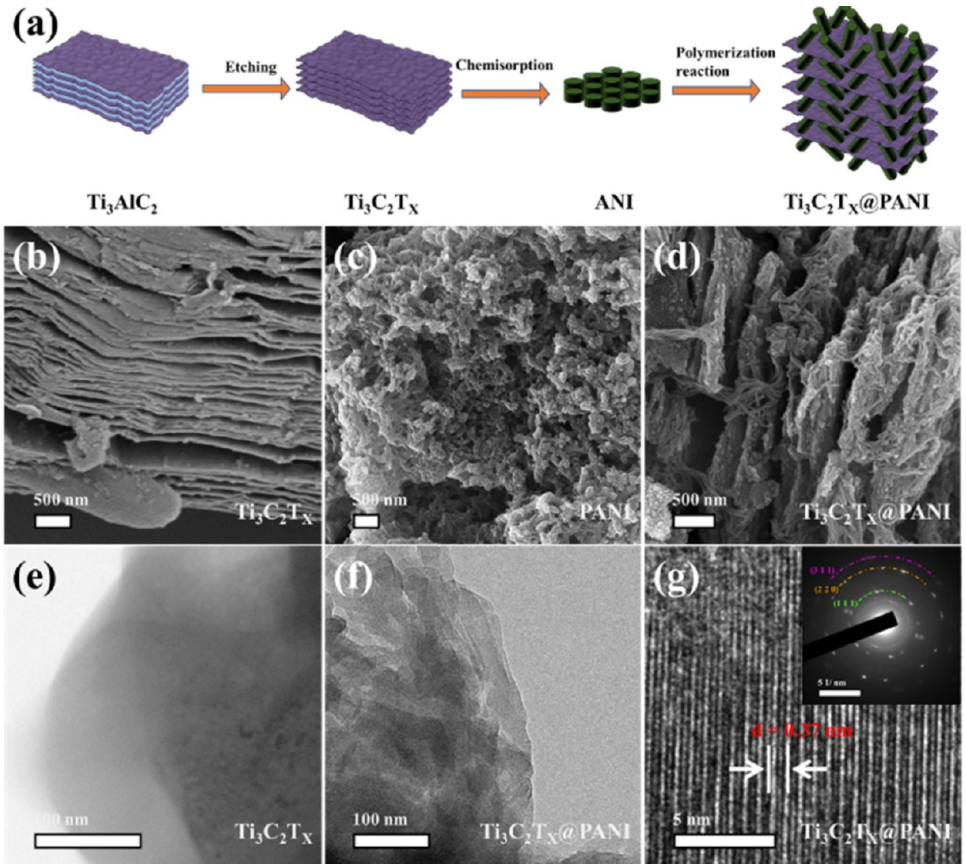

Figure 1. (a) Schematic illustration of the preparation procedure of $Ti_3C_2T_X$@PANI. Representative SEM images of (b) $Ti_3C_2T_X$, (c) PANI, and (d) $Ti_3C_2T_X$@PANI. Representative TEM images of (e) $Ti_3C_2T_X$ and (f) $Ti_3C_2T_X$@PANI. (g) Representative HRTEM image of $Ti_3C_2T_X$@PANI, the inset within being the SAED patterns.

and the byproducts were removed by acid leaching in concentrated HNO_3 (98.0%) for 1 h to obtain a 3D DRGO hydrogel.

Structural Characterization. The topography of samples was investigated by scanning electron microscopy (SEM) (Zeiss, GeminiSEM 300) and transmission electron microscopy (TEM) (FEI, Talos F200S) measurements. X-ray diffraction (XRD) patterns were obtained with a Rigaku Ultima IV X-ray diffractometer (λ = 0.15418 nm). Raman spectra were acquired by using a HORIBA Scientific LabRAM HR Evolution spectrometer with laser excitation at 532 nm. X-ray photoelectron spectroscopy (XPS) analysis was performed by using a Thermo Scientific K-Alpha spectrometer. Thermogravimetric analysis (TGA) was conducted with a TGA5500 instrument. N_2 adsorption/desorption isotherms were collected with a Micromeritics ASAP2460 instrument, where the specific surface area was estimated via the Brunauer–Emmett–Teller (BET) theory, and the pore size distribution was obtained via the adsorption branch isotherm via the Barrett–Joyner–Halenda (BJH) method.

Electrochemical Measurements. Electrochemical tests, including cyclic voltammetry (CV), constant current charge/discharge (GCD), and electrochemical impedance spectroscopy (EIS), were conducted in a two-electrode system using a CHI 660E electrochemical workstation. A zinc foil was used as the counter electrode, with RGO, $Ti_3C_2T_X$-RGO, $Ti_3C_2T_X$@PANI-RGO, and DRGO hydrogels as the working electrodes, along with 2 M $ZnSO_4$ (99.0%) as the electrolyte and a glass fiber filter paper as the separator to assemble a half cell in the CR2032 button cell. The active material was vacuum-dried at 55 °C (24 h) and subsequently immersed in 2 M $ZnSO_4$ for 24 h to reach electrolyte equilibrium. Due to the excellent mechanical strength of RGO, $Ti_3C_2T_X$-RGO, $Ti_3C_2T_X$@PANI-RGO, and DRGO hydrogels, the active materials were loaded directly onto the nickel foam current collector as working electrodes (loading mass ca. 1.0 mg and active surface area ca. 0.6 cm^{-2}) without binders, which avoids the cumbersome electrode preparation process.

The specific capacitance (C_a), specific capacity (C_y), energy density (E), and power density (P) of the electrode were analyzed by GCD tests using the following equations:

$$C_a = It/mU \tag{1}$$

$$C_y = It/(3.6m) \tag{2}$$

$$E = 0.5CU^2/3.6 \tag{3}$$

$$P = E/(t/3600) \tag{4}$$

where I refers to the current (A), t refers to the discharge time (s), m refers to the mass (g) of active materials of electrodes, and U refers to the potential difference (V).

ZIC Device. A ZIC full cell was constructed using $Ti_3C_2T_X$@PANI-RGO as the negative electrode and DRGO as the positive electrode. ZICs balanced the relative mass of the positive and negative electrodes by conserving the positive and negative charges, as shown in the following equations

$$Q = CVm \tag{5a}$$

$$Q_+ = Q_- \tag{5b}$$

$$m_+/m_- = C_-V_-/C_+V_+ \tag{5c}$$

where Q_+ and Q_- stand for the charge stored at the anode and cathode, C_+ and C_- are the specific capacitance of the anode and cathode in half cells, V_+ and V_- are the voltage windows, and m_+ and m_- are the active material mass in the anode and cathode, respectively.

https://doi.org/10.1021/acsami.3c11035
ACS Appl. Mater. Interfaces 2023, 15, 48416–48430

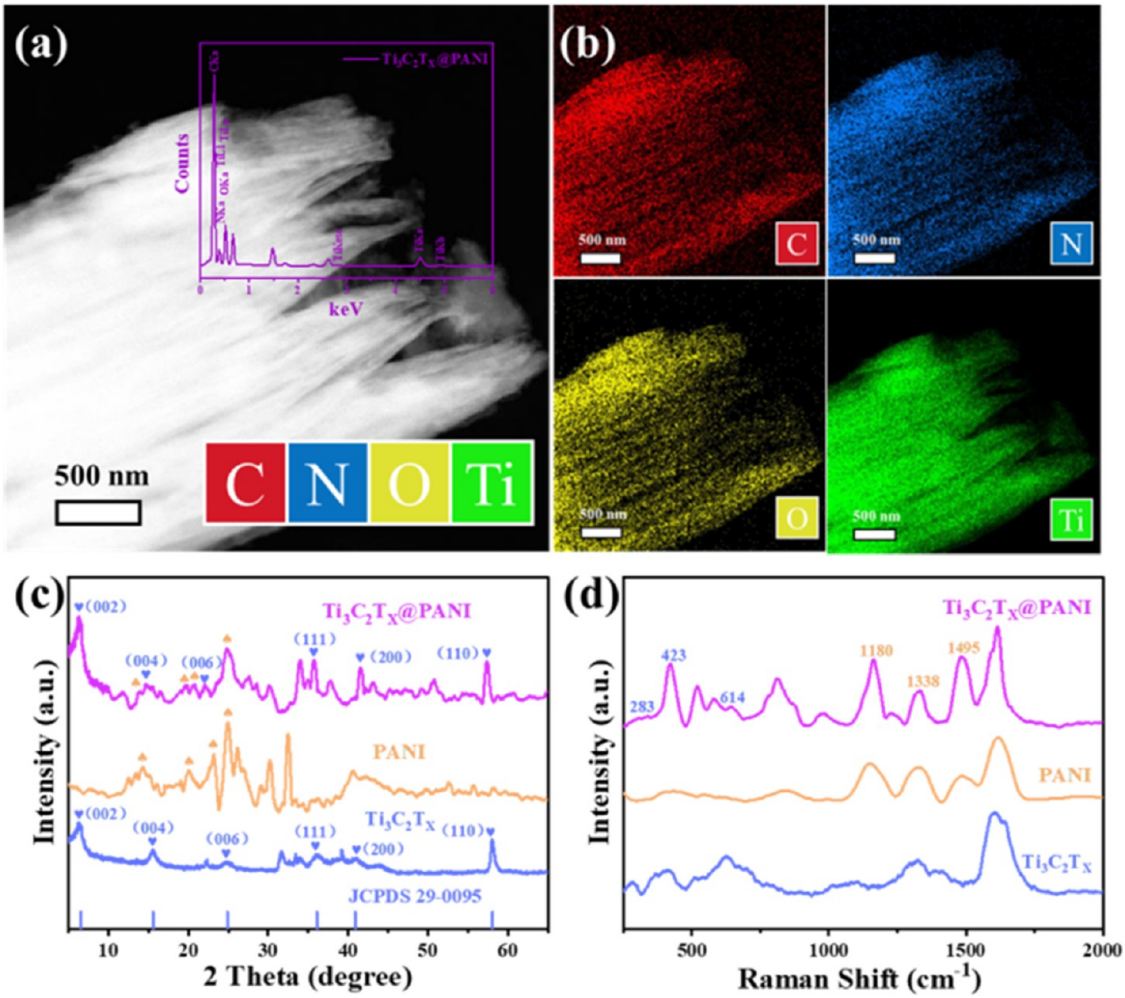

Figure 2. (a) TEM image of $Ti_3C_2T_X$@PANI and (b) related elemental maps of C, N, O, and Ti, with the corresponding EDX spectra in the inset. (c) XRD patterns and (d) Raman spectra of $Ti_3C_2T_X$, PANI, and $Ti_3C_2T_X$@PANI.

RESULTS AND DISCUSSION

$Ti_3C_2T_X$@PANI-RGO Anode. The schematic diagram, as shown in Figure 1a, illustrates the synthesis process of the hierarchical $Ti_3C_2T_X$@PANI heterostructures. First, the $Ti_3C_2T_X$ MXene was prepared by designedly removing the aluminum atomic layers of the MAX phase (Ti_3AlC_2). Next, aniline was adsorbed and chemically oxidized on the surfaces of the $Ti_3C_2T_X$ nanosheets in an ice bath, followed by APS-initiated polymerization in an acidic medium, resulting in the formation of hierarchical 2D $Ti_3C_2T_X$@PANI heterostructures. Figure 1b depicts the 2D multilayer accordion structure of the $Ti_3C_2T_X$ MXene, where the layers were tightly stacked due to the interlayer attraction, likely due to a synergy of van der Waals forces, electrostatic interactions resulting from surface functional groups, and Coulombic interactions stemming from high terminal surface charge densities. High-resolution TEM measurements (Figure 1e) showed that the $Ti_3C_2T_X$ nanosheets possessed a wrinkled sheet structure with a two-dimensional crystal structure. From Figure 1c, one can see that PANI was mostly produced in the form of nanofibers and uniformly intercalated between the layers of the $Ti_3C_2T_X$ nanosheets (Figure 1d) and on the surface of $Ti_3C_2T_X$ (Figure 1f). This led to an expansion of the interlayer spacing and an enhanced specific surface area. In the high-resolution TEM (HRTEM) image (Figure 1g), the $Ti_3C_2T_X$@PANI heterostructures exhibit clearly defined lattice fringes with a distinct interlayer spacing of 0.37 nm, most likely due to $Ti_3C_2T_X$ as PANI is noncrystalline. In the selected area electron diffraction (SAED) patterns (the inset of Figure 1g), three strong rings were identified, corresponding to interplanar distances of 0.25, 0.15, and 0.13 nm, which can be ascribed to the (111), (220), and (311) lattice planes of $Ti_3C_2T_X$, respectively.

EDX analysis provides more structural details of the $Ti_3C_2T_X$@PANI heterostructure. As shown in Figure 2a and the inset, the elements of C, N, O, and Ti can be readily identified, with a rather uniform distribution (Figure 2b), confirming the organized assembly of PANI nanofibers into the $Ti_3C_2T_X$ nanosheets. Further structural insights were gained from XRD and Raman analyses. The XRD patterns of $Ti_3C_2T_X$, PANI, and $Ti_3C_2T_X$@PANI are shown in Figure 2c. The $Ti_3C_2T_X$@PANI heterostructures entail six major diffraction peaks at 2θ = 6.6, 15.6, 24.8, 36.2, 41.0, and 58.3°, consistent with the (002), (004), (006), (111), (200), and (110) crystalline planes of $Ti_3C_2T_X$,[21] respectively, with four additional ones at 15.3, 18, 19.2, and 25.4° due to PANI. Notably, the former were clearly broadened and shifted to lower angles, as compared to those of $Ti_3C_2T_X$ alone, likely due to the intercalation of PANI nanofibers into the $Ti_3C_2T_X$ layers. As shown in Figure 2d, both $Ti_3C_2T_X$ and $Ti_3C_2T_X$@PANI exhibited vibrational peaks at 283, 423, and 614 cm^{-1} due to

https://doi.org/10.1021/acsami.3c11035
ACS Appl. Mater. Interfaces 2023, 15, 48416−48430

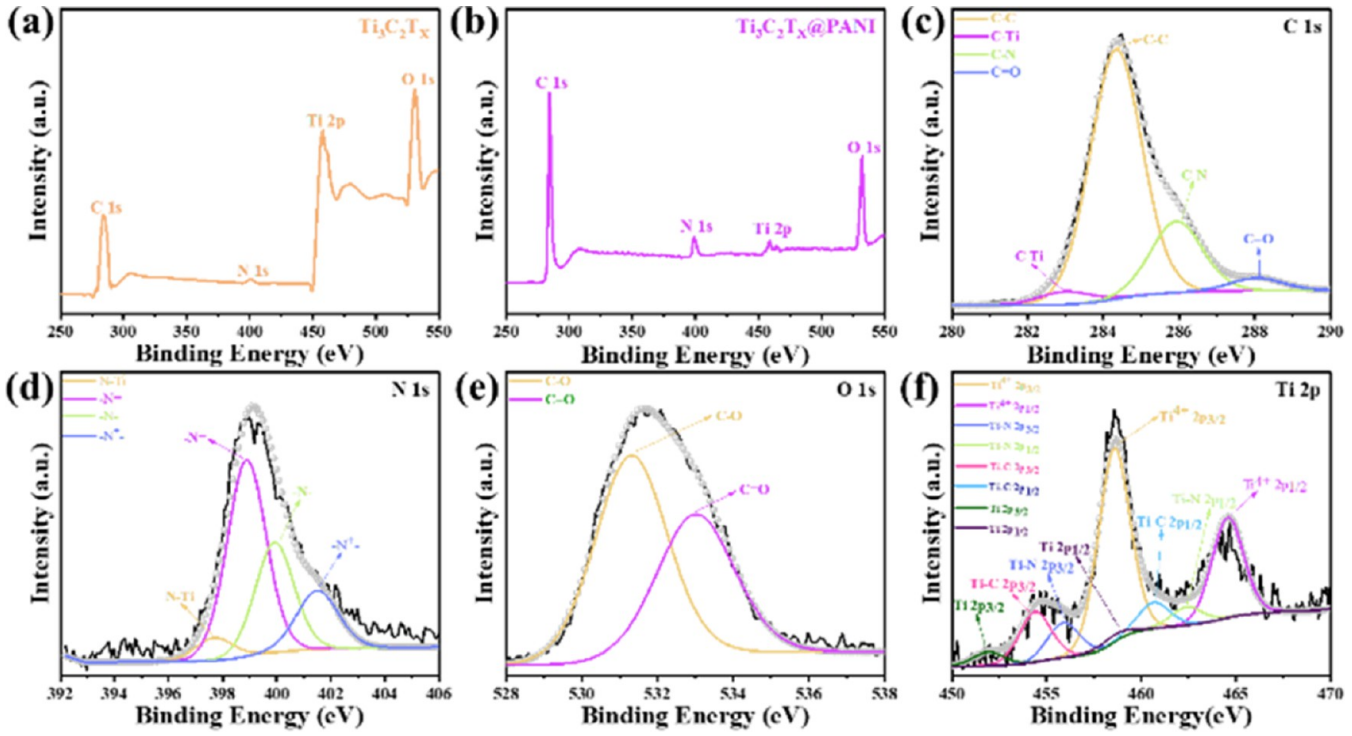

Figure 3. XPS survey spectra of (a) $Ti_3C_2T_X$ and (b) $Ti_3C_2T_X$@PANI. High-resolution spectra of $Ti_3C_2T_X$@PANI: (c) C 1s, (d) N 1s, (e) O 1s, and (f) Ti 2p electrons.

the Ti−C vibrations, and the peaks at 1180, 1338, and 1495 cm^{-1} likely arose from the C−H bending of the quinoid ring, C−N stretching of the benzenoid ring, and C═N stretching of the quinoid of PANI and $Ti_3C_2T_X$@PANI, respectively. Notably, no additional peaks were detected, confirming the homogeneous deposition of PANI nanofibers onto the entire exposed surface of the $Ti_3C_2T_X$ nanosheets.

XPS surveys were then conducted to discuss the elemental composition and chemical bonding of the examples.[49] From the survey spectra, as shown in Figure 3a,b, the C 1s, N 1s, Ti 2p, and O 1s electrons can be detected at approximately 284, 399, 459, and 530 eV in the $Ti_3C_2T_X$ and $Ti_3C_2T_X$@PANI samples, respectively. Notably, an evident increase in the intensity of the N 1s peak is observed in the latter due to the incorporation of PANI into the $Ti_3C_2T_X$ nanosheets. The high-resolution scans of the C 1s, N 1s, O 1s, and Ti 2p electrons for the $Ti_3C_2T_X$@PANI sample are shown in Figure 3c−f. Four peaks can be resolved in the C 1s spectrum at 283, 284.4, 285.9, and 288.1 eV (Figure 3c) and assigned to C−Ti, C−C, C−N, and C═O, respectively. From the N 1s spectrum (Figure 3d), the N−Ti, −N═, −N−, and $-N^+-$ peaks can be found at 398.1, 398.9, 399.9, and 401.5 eV, respectively, arising from the PANI nanofibers. The spectra of the O 1s electrons are shown in Figure 3e, with two peaks at 531.3 eV (C−O) and 533 eV (C═O). Figure 3f presents the Ti 2p spectrum, where the $2p_{3/2}$/$2p_{1/2}$ doublets can be deconvoluted at 451.9/458.5 eV for metallic Ti, 454.4/460.7 eV for Ti−C, 455.9/462.4 eV for Ti−N, and 458.6/464.6 eV for Ti^{4+}.

GO, a strong gelatinous cross-linking agent, was then employed to assemble the $Ti_3C_2T_X$@PANI heterostructures into 3D porous cross-linked RGO hydrogels via a hydrothermal approach (Figure 4a). A 3D $Ti_3C_2T_X$@PANI-RGO hydrogel was synthesized by chemically interacting exterior oxygen-containing groups of $Ti_3C_2T_X$ with RGO nanosheets reduced from GO by using L-ascorbic acid (Figure 4b). The superior mechanical properties of the hydrogels enabled the direct preparation of electrode sheets, avoiding the complex preparation of slurries and the interference with electrochemical properties by conductive agents and inert adhesives. In comparison to $Ti_3C_2T_X$@PANI, $Ti_3C_2T_X$@PANI-RGO hydrogels show a broadened half-peak width of several XRD diffraction peaks, along with a leftward shift in the peak position (Figure 4c), suggesting a further enlarged interlayer spacing of the $Ti_3C_2T_X$@PANI-RGO hydrogel.

The N_2 adsorption/desorption isotherms of $Ti_3C_2T_X$@PANI are depicted in Figure 4d. The absence of a mesoporous distribution within the medium pressure range is evident from the low adsorption volume, and the isotherms indicate a supreme adsorption capacity at $P/P0 = 1$, indicative of the formation of macropores. By contrast, the $Ti_3C_2T_X$@PANI-RGO hydrogel exhibited a type IV isotherm and a pronounced type H2 hysteresis loop (Figure 4e), suggesting the formation of mesopores in the relative pressure range of 0.1−1.0. And the BET specific surface area of the $Ti_3C_2T_X$@PANI-RGO hydrogel was estimated to be 264.79 $m^2\ g^{-1}$, about 60 times that of $Ti_3C_2T_X$@PANI (4.86 $m^2\ g^{-1}$). These results show that the specific surface area of the $Ti_3C_2T_X$@PANI nanosheets was expanded by the 3D frameworks of RGO. The BJH theory was used to analyze pore size distributions of $Ti_3C_2T_X$@PANI and the $Ti_3C_2T_X$@PANI-RGO hydrogel. The inset of Figure 4d shows that the $Ti_3C_2T_X$@PANI powder was mainly composed of micropores at 1.72 and 2.04 nm. For comparison, the $Ti_3C_2T_X$@PANI-RGO hydrogel possessed a broad mesoporous size distribution, with significantly larger pore volumes at pore sizes of 3.57, 7.75, and 20.39 nm (the inset of Figure 4e). These findings suggest that the combination of $Ti_3C_2T_X$@PANI and RGO consisted of a 3D porous cross-linked structure characterized by random pores and thin pore walls. This

https://doi.org/10.1021/acsami.3c11035
ACS Appl. Mater. Interfaces 2023, 15, 48416−48430

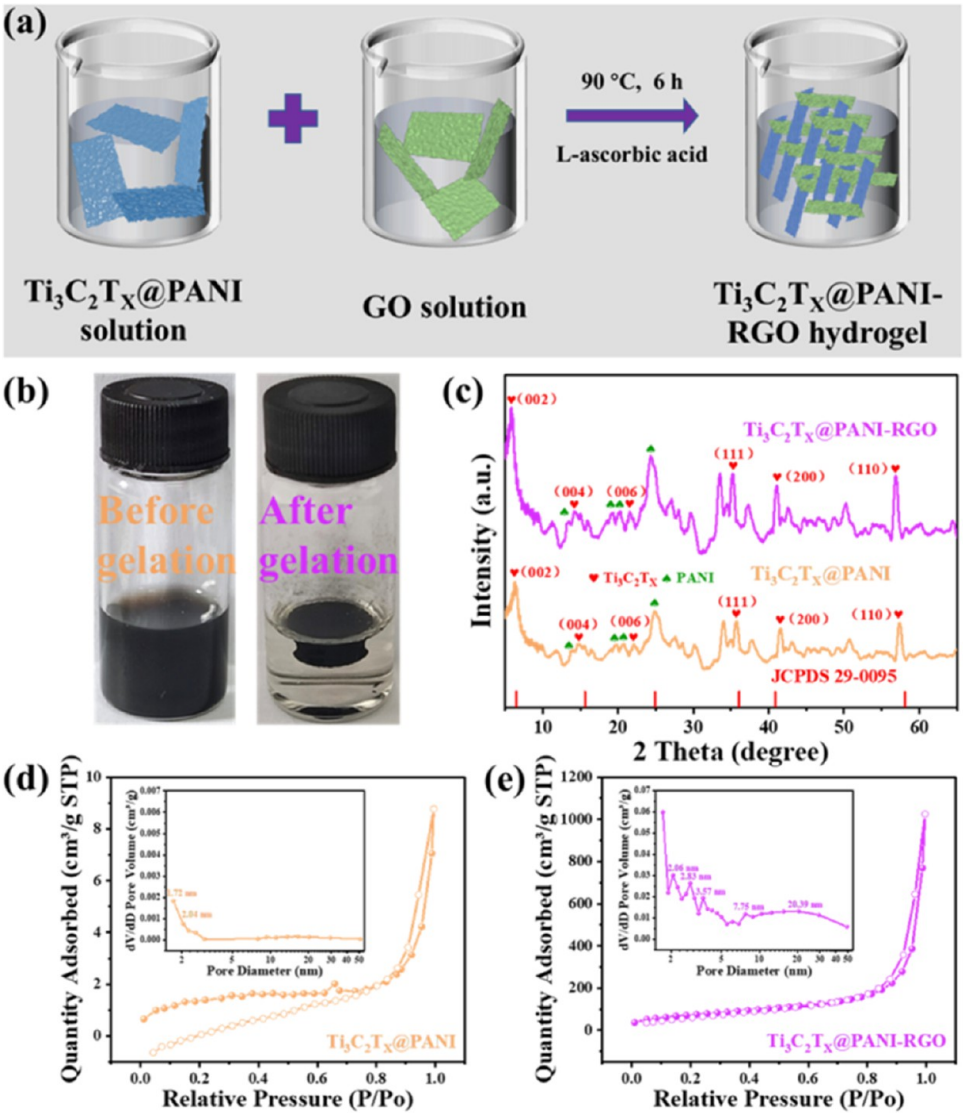

Figure 4. (a) Schematic illustration of the producing approach of $Ti_3C_2T_X$@PANI-RGO. (b) Photos of the $Ti_3C_2T_X$@PANI/GO colloid before and after reaction. (c) XRD patterns of $Ti_3C_2T_X$@PANI and the $Ti_3C_2T_X$@PANI-RGO hydrogel. Typical N_2 adsorption/desorption isotherms of (d) $Ti_3C_2T_X$@PANI and (e) the $Ti_3C_2T_X$@PANI-RGO hydrogel. The insets are the corresponding pore size distributions.

unique architecture offers several benefits, including reduced aggregation of $Ti_3C_2T_X$, improved conductivity, and increased employment of active surface areas of the $Ti_3C_2T_X$@PANI-RGO hydrogel in electrochemical applications.

Figure 5a depicts the CV curves of RGO, $Ti_3C_2T_X$-RGO, and $Ti_3C_2T_X$@PANI-RGO electrodes in a two-electrode system at a potential scan rate of 10 mV s^{-1}. All CV curves exhibited a closed figure with no crossing or coincidence. The voltage range of the $Ti_3C_2T_X$@PANI-RGO heterostructure hydrogel electrodes was 0−2.0 V, obviously larger than that of RGO and $Ti_3C_2T_X$-RGO (0−1.6 V). Moreover, the $Ti_3C_2T_X$@PANI-RGO heterostructure hydrogel electrode exhibited a significantly larger CV curve integration area than that of RGO and $Ti_3C_2T_X$-RGO (approximately 5.91 times the former and 4.51 times the latter), indicating a drastically stronger capacitance performance and faster reaction kinetics. This confirms the feasibility of imbedding PANI nanofibers between the $Ti_3C_2T_X$ nanosheets. Distinct redox peaks appear in the CV plots of the $Ti_3C_2T_X$@PANI-RGO heterostructure hydrogels, demonstrating that RGO and $Ti_3C_2T_X$ mainly provided EDLC during the charge/discharge process, while the complex internal structure of PANI provided pseudocapacitance due to the redox reactions. Figure 5b shows the CV curves of the $Ti_3C_2T_X$@PANI-RGO heterostructure hydrogel electrodes at different scan rates. As the potential scanning rate increased, there was a slight shift of the oxidation−reduction peak due to inevitable irreversible polarization. However, the lack of a significant change in the curves indicated significant reaction rate stability, high reversibility, and low equivalent series resistance.

As shown in Figure 5c, the charge storage capacity is further examined by measuring the GCD curves at a current density of 1 A g^{-1}. Although the $Ti_3C_2T_X$@PANI-RGO hydrogel electrodes showed a wider potential window, the discharge time was longer. Furthermore, the specific capacitance of the $Ti_3C_2T_X$@PANI-RGO hydrogel electrodes (406.52 F g^{-1}) was significantly higher than that of the $Ti_3C_2T_X$-RGO electrode (153.12 F g^{-1}) and RGO electrode (90.83 F g^{-1}) at a current density of 1 A g^{-1}. This indicates enhanced charge storage of the highly conductive 3D RGO configuration for gelling $Ti_3C_2T_X$@PANI heterostructures, in agreement with CV

https://doi.org/10.1021/acsami.3c11035
ACS Appl. Mater. Interfaces 2023, 15, 48416−48430

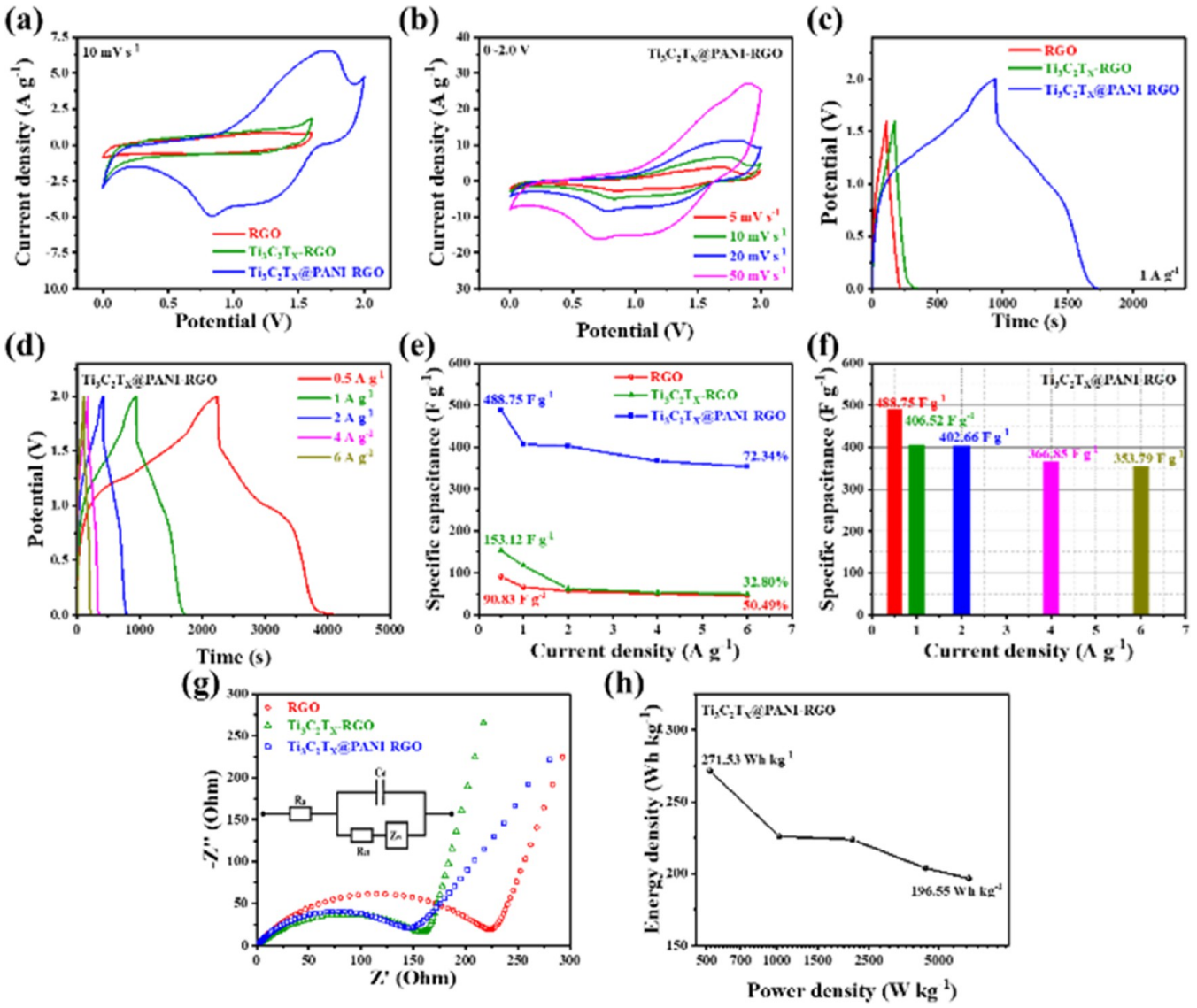

Figure 5. (a) CV profiles of RGO, $Ti_3C_2T_X$-RGO, and $Ti_3C_2T_X$@PANI-RGO at a scan rate of 10 mV s^{-1}. (b) CV profiles of $Ti_3C_2T_X$@PANI-RGO at different scan rates. (c) GCD profiles of RGO, $Ti_3C_2T_X$-RGO, and $Ti_3C_2T_X$@PANI-RGO at a current density of 1 A g^{-1}. (d) GCD curves of $Ti_3C_2T_X$@PANI-RGO electrodes at different current densities. (e) Plots of specific capacitance vs current density of RGO, $Ti_3C_2T_X$-RGO, and $Ti_3C_2T_X$@PANI-RGO. (f) Specific capacitances calculated via the GCD data at diverse current densities. (g) Nyquist impedance plots of RGO, $Ti_3C_2T_X$-RGO, and $Ti_3C_2T_X$@PANI-RGO, with the equivalent circuits shown in the inset. (h) Ragone curve of $Ti_3C_2T_X$@PANI-RGO.

analysis. All GCD curves of the RGO, $Ti_3C_2T_X$-RGO, and $Ti_3C_2T_X$@PANI-RGO hydrogels are quasitriangular, indicating the synergy of EDLC and pseudocapacitance. Figure 5d displays the GCD curves of the ZIC with $Ti_3C_2T_X$@PANI-RGO heterostructure hydrogels as the anodes at different current densities. In the current density range of 0.5−6 A g^{-1}, the GCD curves of the $Ti_3C_2T_X$@PANI-RGO heterostructure hydrogels showed no significant *iR* reduction, evidencing fast electron transfer and electrolyte ion diffusion within the electrodes. Moreover, the high symmetry of the GCD curves suggests a small irreversible equivalent resistance and low electrical energy loss during charging and discharging and hence a favorable electrochemical performance of the electrode under high current density. The rate performance of the RGO, $Ti_3C_2T_X$-RGO, and $Ti_3C_2T_X$@PANI-RGO hydrogels is shown in Figure 5e. With the increase of the current density, the attenuation of the specific capacitance accelerates. RGO, $Ti_3C_2T_X$-RGO, and $Ti_3C_2T_X$@PANI-RGO showed a specific capacitance of 90.83, 153.12, and 488.75 F g^{-1} at the current density of 0.5 A g^{-1}, respectively, and 50.49, 32.80, and 72.34% of the specific capacitance was retained at 6 A g^{-1}, respectively. This shows the stable and outstanding rate performance of the $Ti_3C_2T_X$@PANI-RGO hydrogels. The specific capacitance of the $Ti_3C_2T_X$@PANI-RGO heterostructure hydrogel at different current densities is shown in Figure 5f.

The samples then underwent EIS tests within the frequency range of 10^{-2}−10^5 Hz (Figure 5g, with the equivalent circuit shown in the inset). The semicircle in the high-frequency region is attributed to the charge-transfer resistance (R_{ct}), whereas the linear portion of the low-frequency region is due to the Warburg resistance (W_d) of material diffusion. From the EIS data, the RGO, $Ti_3C_2T_X$-RGO, and $Ti_3C_2T_X$@PANI-RGO hydrogels can be seen to exhibit an R_{ct} of 229.7, 168.5, and 150.1 Ω, respectively. This suggests enhanced electron-transfer kinetics and reduced reaction irreversibility. Additionally, the serial resistances (R_s) of RGO, $Ti_3C_2T_X$-RGO, and $Ti_3C_2T_X$@

https://doi.org/10.1021/acsami.3c11035
ACS Appl. Mater. Interfaces 2023, 15, 48416−48430

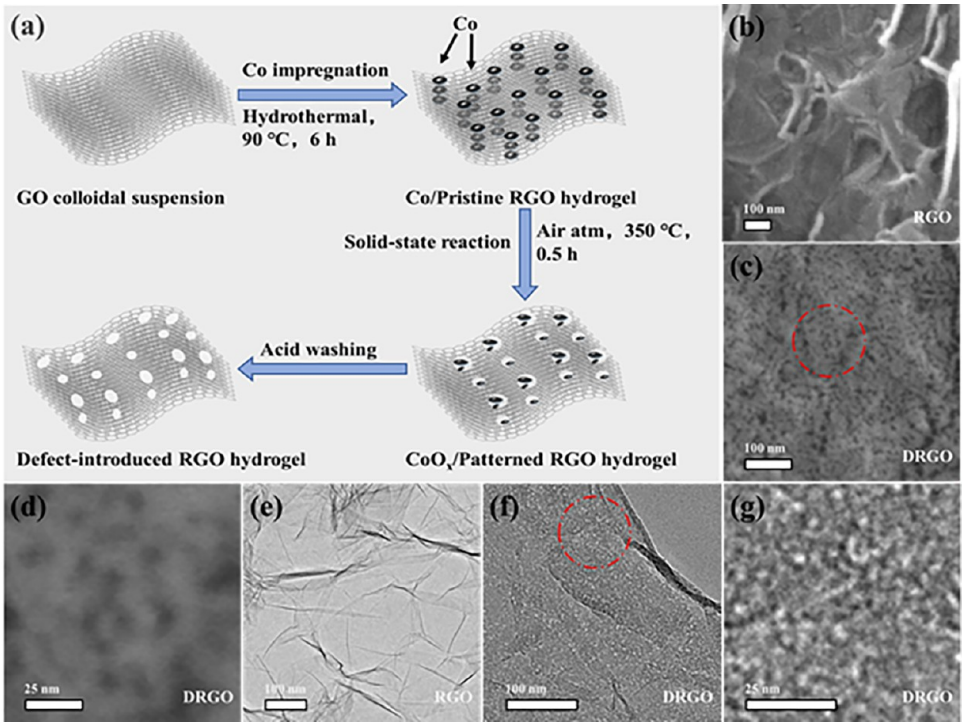

Figure 6. (a) Schematic diagram of the fabrication procedure of DRGO. SEM images of (b) RGO and (c) DRGO. (d) Zoom-in image of the circular region in panel (c). TEM images of (e) RGO and (f) DRGO. (g) Zoom-in image of the circular region in panel (f).

PANI-RGO hydrogels were estimated to be 0.76, 0.70, and 0.64 Ω, respectively, indicative of good electrical conductivity of the samples. Furthermore, the linear segment shows that the $Ti_3C_2T_X$@PANI-RGO hydrogel showed a slope lower than that of RGO and $Ti_3C_2T_X$-RGO, indicating more significant pseudocapacitance characteristics. As shown in the Ragon plot of $Ti_3C_2T_X$@PANI-RGO (Figure 5h), an ultrahigh energy density of 271.53 Wh kg^{-1} was obtained at 516.0 W kg^{-1} and 196.55 Wh kg^{-1} at 6725.98 W kg^{-1}.

It is well known that the high electric conductivity of active materials is conducive to fast electrochemical reaction kinetics, a key contribution to the excellent cycling capability and quick rate charge−discharge property. Thus, the remarkable electrochemical performance of the $Ti_3C_2T_X$@PANI-RGO heterostructure hydrogel can be attributed to the synergistic effect among the structural components and the 3D architecture. Specifically, the conductive $Ti_3C_2T_X$ substrate provided both abundant transport channels for ions and active interfacial centers, while the fiber-shaped PANI increased the pseudocapacitance and promoted the diffusion of electrolyte ions. In addition, the 3D structure allowed for fast electrolyte ion diffusion and intimate contact of the $Ti_3C_2T_X$@PANI-RGO hydrogel with the electrolyte solution, leading to a high rate capability.

DRGO Cathode. 3D DRGO hydrogels were synthesized by using a simple cobalt-catalyzed gasification strategy, as depicted in Figure 6a. First, a mild hydrothermal self-assembly strategy was employed to prepare a Co-doped graphene oxide colloid solution at 90 °C. Subsequently, at 350 °C, the metal Co was oxidized into Co oxide and then catalytically gasified with C to generate plentiful defects on the surface of RGO ($6CoO + O_2 \rightarrow 2Co_3O_4$; $Co_3O_4 + C \rightarrow 3CoO + CO$). Finally, the products were subjected to boiling nitric acid washing to remove impurities. In the SEM image (Figure 6b), the RGO nanosheets can be seen to possess a morphology of wrinkled layers and a clear cross-linked structure. DRGO exhibited a similar structure with abundant mesopores (Figure 6c,d). Prior to the patterning process, the graphitic structure of RGO appeared almost intact (Figure 6e). And after defect engineering, a large amount of cavities was evenly distributed on the surface of DRGO (Figure 6f,g). These results indicate that DRGO retained the stable graphite structure of RGO while simultaneously increasing the specific surface area and porosity, a unique structural feature for enhanced capacitance performance.

XRD and Raman measurements were carried out to examine the functional alterations of RGO and DRGO. From the XRD patterns of RGO and DRGO, as shown in Figure 7a, the diffraction peaks at 2θ = 25.04 and 43.06° of RGO can be attributed to the (002) and (100) planes of graphite, respectively;[38] while the diffraction peaks of DRGO were somewhat widened and shifted to a lower angle at 2θ = 23.68 and 42.99°. This indicates an expanded layer spacing of 3D DRGO that was conducive to inhibiting graphene layer stacking. From the Raman spectra, as shown in Figure 7b, the D band (1350 cm^{-1}), G band (1586 cm^{-1}), and 2D band (2697 cm^{-1}) can be readily identified. The corresponding D and G band intensity ratio (I_D/I_G) was estimated to be 1.15 for DRGO, significantly higher than that of RGO (0.92), suggesting increasingly defective structures in the former due to the cocatalytic cavity generation. Figure 7c,d show the N_2 adsorption/desorption isotherms of RGO and DRGO. The former is a type II isotherm that rose rapidly at relatively low pressures, with a certain number of macropores (Figure 7c). In contrast, the medium relative pressure range of DRGO showed a type IV isotherm, indicating the formation of mesopores (Figure 7d). 3D DRGO exhibited a type H1 hysteresis loop, indicating an even mesoporous pore size distribution and inerratic pore structure. According to the BET method, the specific surface area was estimated to be 78.73 m^2 g^{-1} for the

https://doi.org/10.1021/acsami.3c11035
ACS Appl. Mater. Interfaces 2023, 15, 48416−48430

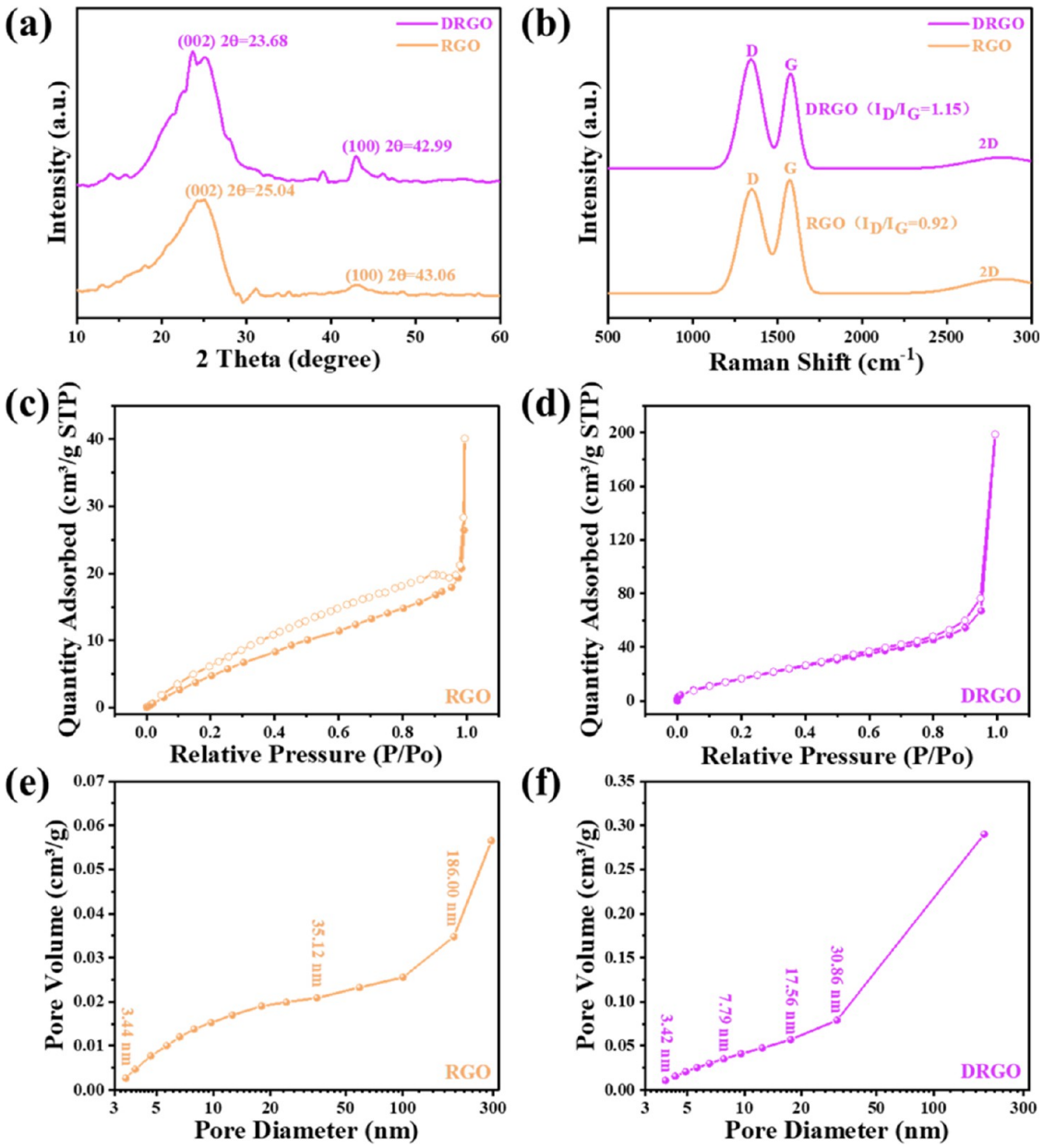

Figure 7. (a) XRD patterns and (b) Raman spectra of RGO and DRGO. N_2 adsorption/desorption isotherms of (c) RGO and (d) DRGO. Pore size distributions of (e) RGO and (f) DRGO.

3D DRGO hydrogel, approximately 2.46 times that of RGO (31.97 m^2 g^{-1}).

The pore size distributions of RGO and DRGO were calculated using the BJH method and are depicted in Figure 7e,f. The primary distribution of RGO (Figure 7e) had a mesoporous pore size of 3.44 and 35.12 nm and a large pore size of 186.00 nm, and the pore volume and average pore sizes were 0.0566 cm^3 g^{-1} and 3.44 nm, respectively. Besides, the pore sizes of 3D DRGO (Figure 7f) were primarily at 3.42, 7.79, 17.56, and 30.86 nm, and the pore volume and average pore size were 0.2901 cm^3 g^{-1} and 3.42 nm, respectively. The pore volume of DRGO was 1 order of magnitude larger than that of RGO and more widely distributed in the mesoporous range (2−50 nm). These results suggest that 3D DRGO helped alleviate tight stacking between sheets, increase electrochemically reactive surfaces, and improve conductivity.

The TGA curves are illustrated in Figure 8a, with RGO and DRGO retaining 72.67 and 48.23% of their weight, respectively. At temperatures below 260.93 °C, the weight losses of RGO and DRGO were similar. However, at higher temperatures, the decline of the RGO curve was significantly greater than that of DRGO, indicating the superior thermal stability of 3D DRGO. This may be ascribed to the unstable functional groups around the edges of RGO and oxygen-containing groups on the surface, which were susceptible to water adsorption and easily decomposed at high temperatures. Yet, after washing and high-temperature treatment, these groups vanished from 3D DRGO, leading to improved thermal stability.

Figure 8b shows the CV graphs of the RGO and DRGO hydrogels at 10 mV s^{-1}, which display a closed loop. The potential window of DRGO (0−1.8 V) was greater than that of RGO (0−1.6 V) and the integrated area of the CV curve was approximately 4 times that of RGO. This suggests that DRGO

https://doi.org/10.1021/acsami.3c11035
ACS Appl. Mater. Interfaces 2023, 15, 48416−48430

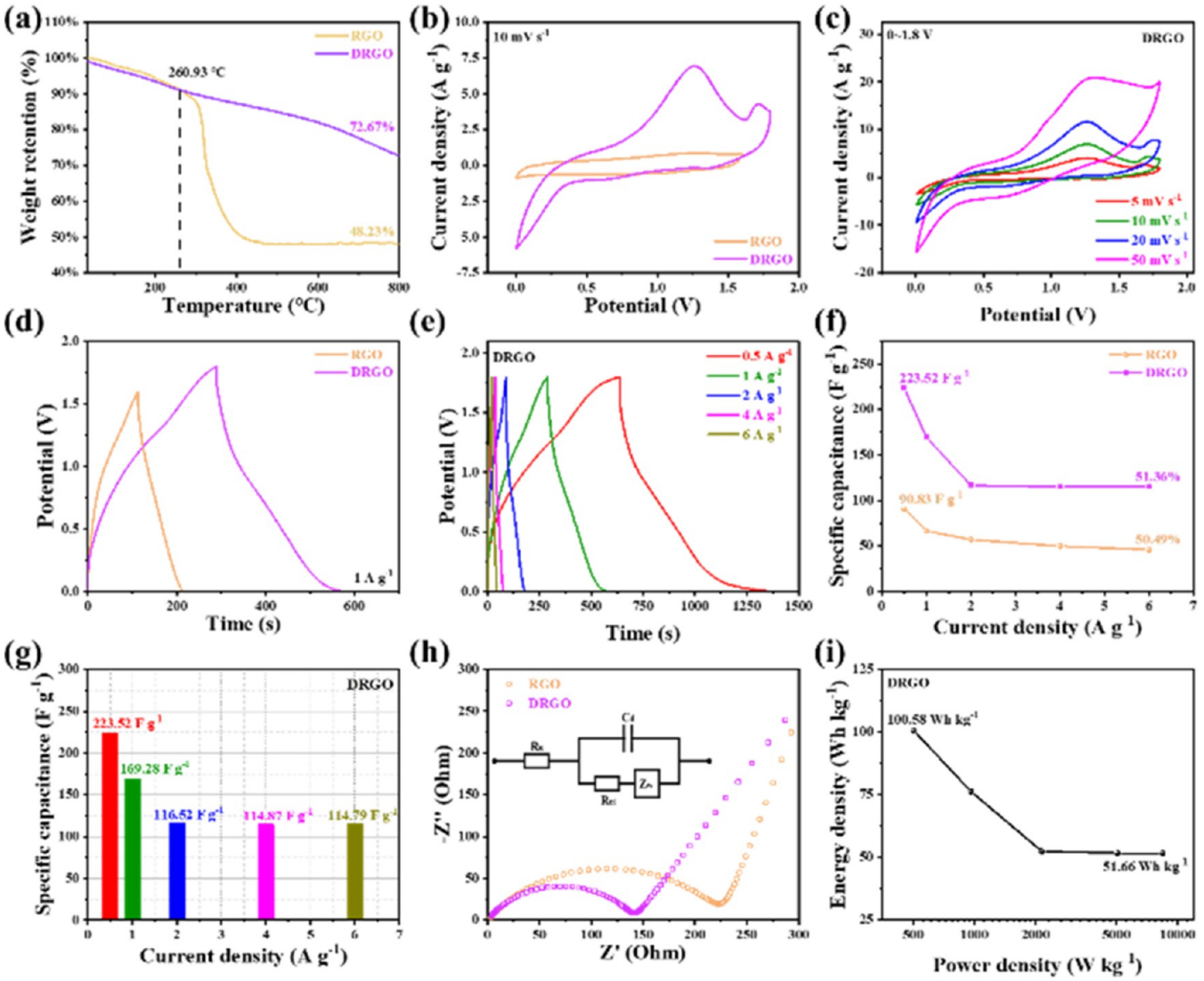

Figure 8. (a) TGA curves of the original RGO and DRGO. (b) CV profiles of RGO and DRGO at a scan rate of 10 mV s^{-1}. (c) CV profiles of DRGO at different scan rates. (d) GCD profiles of RGO and DRGO at a current density of 1 A g^{-1}. (e) GCD profiles of DRGO at different current densities. (f) Specific capacitance vs current density curve of RGO and DRGO. (g) Specific capacitances calculated via GCD data at different current densities. (h) Nyquist impedance curves of RGO and DRGO, with the equivalent circuit shown in the inset. (i) Ragone plot of DRGO.

possessed faster ion transport kinetics and superior charge storage capacity. The CV of DRGO also exhibited clear redox peaks, indicating both capacitance contribution and diffusion control contribution during charge storage.

The CV curves of the 3D DRGO hydrogel electrodes at different scan rates are depicted in Figure 8c. The similarity in the curvature of all CV curves indicates excellent rate stability of 3D DRGO during the charge and discharge processes. This suggests that the patterning process of 3D DRGO was selective and occurred mostly on the carbon atoms that interacted with Co oxide, thereby preserving the fundamental structure and high conductivity of the graphite carbon. Nevertheless, there is no crossover or overlap of the curves, demonstrating that 3D DRGO facilitated fast ion diffusion, low irreversibility, and low series resistance.

The GCD curves of RGO and DRGO at a current density of 1 A g^{-1} are presented in Figure 8d. The 3D DRGO hydrogel electrodes exhibited a considerably longer discharge time and higher capacitance (169.28 F g^{-1}) than RGO. These results indicate that the introduction of defects through the Co cocatalytic gasification strategy markedly improved the charge storage performance, which is consistent with the findings from the CV profiles. Figure 8e shows the GCD curves of the 3D DRGO hydrogels acting as the positive electrode at a current density of 0.5−6 A g^{-1}. These GCD graphs showed no significant *iR* drop, indicating efficient electron transfer and electrolyte ion diffusion within electrodes. Moreover, all GCD curves exhibited high symmetry, signifying a high degree of reaction reversibility and the absence of considerable polarization during charge/discharge.

The specific capacitance of RGO and 3D DRGO at a current density of 0.5−6 A g^{-1} is shown in Figure 8f. The specific capacitance of 3D DRGO at a current density of 0.5 A g^{-1} was 223.52 F g^{-1}, while 51.36% of the specific capacitance was retained at 6 A g^{-1}, substantially better than that of RGO. This shows the excellent chemical stability and rate performance of the 3D DRGO hydrogels. Figure 8g shows the specific capacitance of the 3D DRGO hydrogels at different current densities. Nyquist plots of the RGO and DRGO hydrogels are similar in form (Figure 8h, the inset shows the equivalent

https://doi.org/10.1021/acsami.3c11035
ACS Appl. Mater. Interfaces 2023, 15, 48416−48430

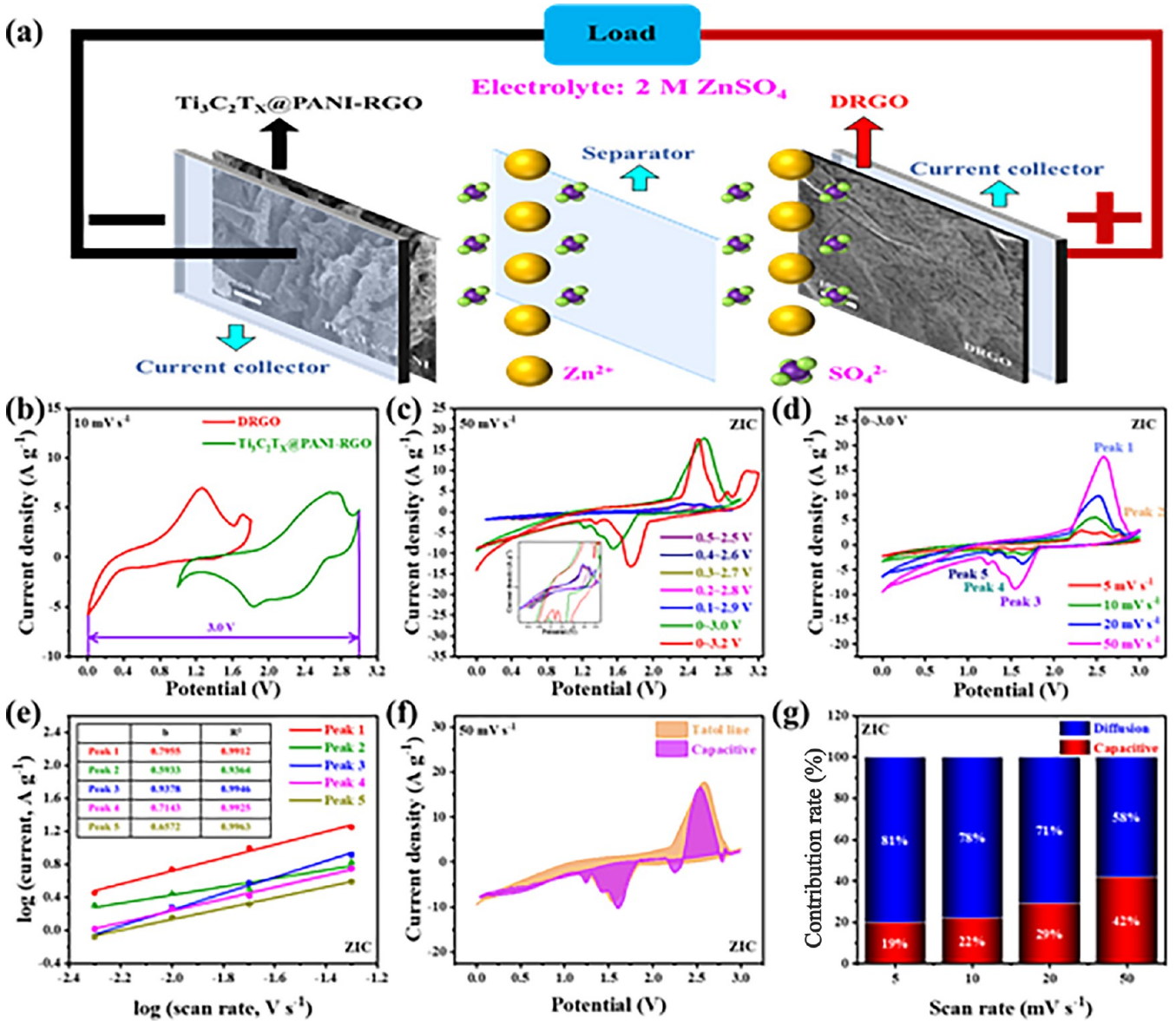

Figure 9. (a) Schematic illustration of the DRGO//$Ti_3C_2T_X$@PANI-RGO ZIC device. (b) CV profiles of an individual DRGO cathode and a $Ti_3C_2T_X$@PANI-RGO anode at a scan rate of 10 mV s^{-1}. (c) CV profiles of the ZIC device at 50 mV s^{-1} with diverse potential windows. The inset is the zoom-in image of the CV curves. (d) CV profiles of the ZIC device at different scan rates. (e) Fitting plots between log(i) and log(v). (f) CV profile with the related capacitive contribution at 50 mV s^{-1}. (g) Capacitive and diffusion contributions at diverse sweep rates.

circuit). The R_{ct} and R_s after the 3D DRGO hydrogel treatment were 141.3 and 0.69 Ω, respectively, which were smaller than those of RGO. This shows that defect engineering led to a markedly reduced series resistance of DRGO and enhanced performance of electrolyte ion transfer. As shown in the Ragon plot (Figure 8i), 3D DRGO exhibited a high energy density of 100.58 Wh kg^{-1} at 501.87 W kg^{-1} and retained an energy density of 51.66 Wh kg^{-1} even at 8453.34 W kg^{-1}.

In summary, the high performance of the 3D DRGO hydrogel electrode can be ascribed to the mesoporous structure that not only provided abundant pathways for speedy ionic/electron diffusion but also impeded the restacking of DRGO and increased the surface utilization.

DRGO//$Ti_3C_2T_X$@PANI-RGO ZIC. A ZIC with a potential window of 3.0 V was constructed by using $Ti_3C_2T_X$@PANI-RGO and DRGO as the negative and positive electrodes, respectively, 2 M $ZnSO_4$ as the electrolyte, and glass fiber filter papers as the diaphragms (Figure 9a). This DRGO//$Ti_3C_2T_X$@PANI-RGO ZIC device exhibited the best electrochemical performance when the charge of the positive and negative electrodes was conserved. According to the charge balance formula (eq 4), the positive to negative electrode mass ratio was optimized to 2.4:1 (total active material of 3.4 mg). During the charging/discharging processes of the ZIC, the electrolyte ions underwent a capacitance process of adsorption/desorption at the cathode and a diffusion-controlled process of intercalation/deintercalation at the anode. The Zn^{2+} ions of the $ZnSO_4$ electrolyte were transferred to the anode during charging and to the cathode during discharging. As shown in Figure 9b, the potential window of the $Ti_3C_2T_X$@PANI-RGO and DRGO electrodes was 2.0 and 1.8 V, respectively, which largely determined the potential window of the DRGO//$Ti_3C_2T_X$@PANI-RGO ZIC device.

https://doi.org/10.1021/acsami.3c11035
ACS Appl. Mater. Interfaces 2023, 15, 48416−48430

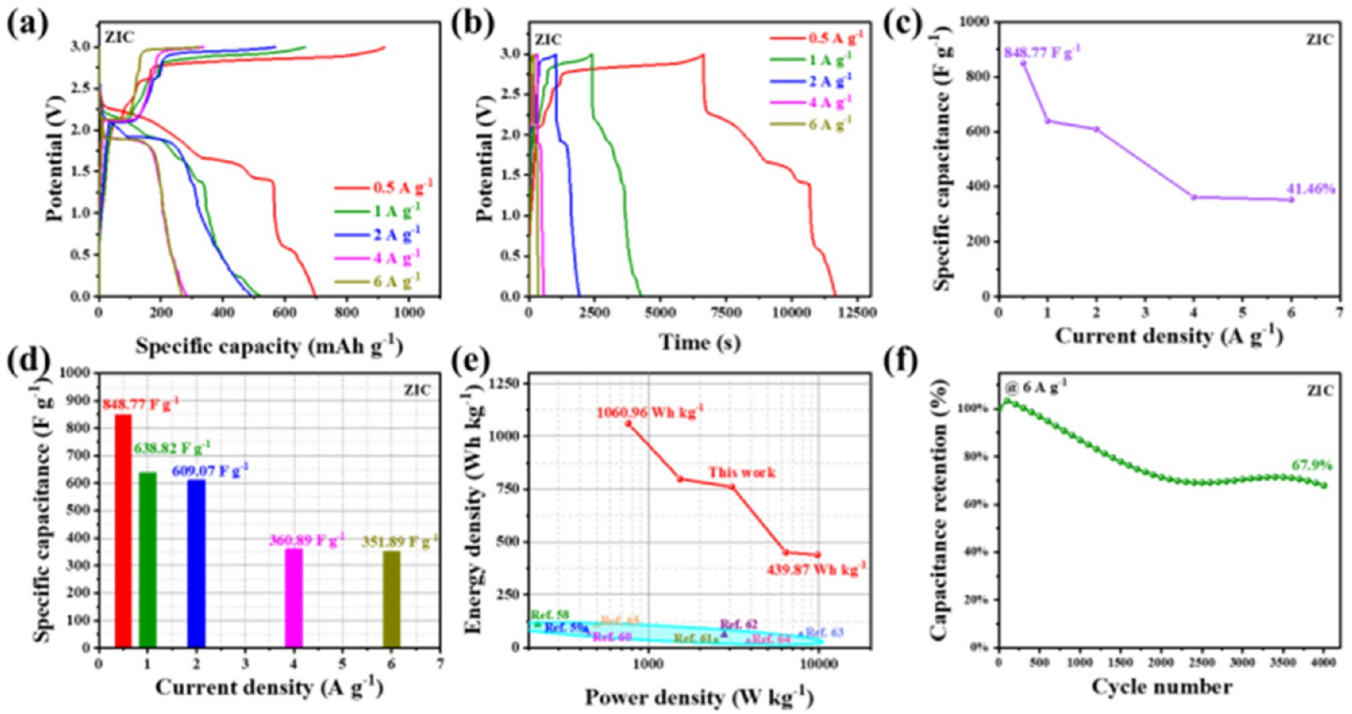

Figure 10. (a) GCD profiles of the ZIC device at different current densities, with the horizontal axis representing specific capacity. (b) GCD profiles of the ZIC device at different current densities, with the horizontal axis representing time. (c) Rate performance plot of the ZIC device. (d) Specific capacitance vs current density plot of the ZIC device. (e) Ragone plot of the ZIC device. (f) Cycling stability of the ZIC device at 6 A g^{-1} for 4000 cycles.

Figure 9c shows the CV plots of the DRGO//$Ti_3C_2T_X$@PANI-RGO ZIC within different voltage windows at 50 mV s^{-1}, and it is worth noting that the curves did not close or cross when the operating voltage range was no more than 3.0 V (in the voltage window of 0−3.2 V, the CV curve crossed). This shows that the operational potential of the ZIC device could be stably extended to 0−3.0 V. The CV profiles of this DRGO//$Ti_3C_2T_X$@PANI-RGO ZIC at scan rates of 5, 10, 20, and 50 mV s^{-1} are shown in Figure 9d. It can be seen that the redox peak positions of the CV curves showed a slight shift as the scanning rate increased, due to the small uncompensated resistance that is inevitable in the time of the charging/discharging process. The CV curve of the ZIC exhibited 5 distinct redox peaks, indicating that the electrochemical reaction of the device underwent a continuous multistep phase transition. At the same time, this is closely related to the synergistic effect of electric double-layer capacitance, pseudocapacitance, and diffusion control of the ZIC during charging and discharging. In addition, the shape of the CV curve remained almost unchanged as the scanning rate increased, indicating that this ZIC device displayed rapid electrolyte permeation and ion transfer.

The CV curves at different scanning rates can further explore the electrochemical reaction mechanism of the ZIC. The charge storage behavior can be analyzed using the following equation, $i = av^b$, where i stands for peak current, v is sweeping rate, and a and b are two adjustable parameters. Generally, it is $b = 0.5$ for a diffusion-controlled process, $0.5 < b < 1$ for both diffusion-controlled and capacitance-controlled processes, and $b \geq 1$ for a capacitance-controlled process. The fitting results of the b values of the DRGO//$Ti_3C_2T_X$@PANI-RGO ZIC are shown in Figure 9e, and all were greater than 0.5 but less than 1. This confirmed that the charge storage mechanism of the ZIC involved a capacitance effect and diffusion control process, and the high coefficient of determination R^2 close to 1 indicated that the error of the fitting result was extremely small.

In the ZIC device, the contributions of the capacitance and diffusion-controlled processes can also be quantified through the CV curves at different scan rates. The capacitance contribution can be quantified using the following equation, $I = k_1v + k_2v^{1/2}$, where I is the current, k_1v stands for the capacitive contribution, and $k_2v^{1/2}$ stands for the diffusion-controlled process. As shown in Figure 9f, the DRGO//$Ti_3C_2T_X$@PANI-RGO ZIC showed a high capacitance contribution of up to 42% at a scan rate of 50 mV s^{-1}. As shown in Figure 9g, as the scan rate increased, the capacitance contribution of the DRGO//$Ti_3C_2T_X$@PANI-RGO ZIC was positively correlated, and the diffusion control contribution was negatively correlated. The high capacitance contribution greatly enhanced the rate performance of the ZIC.

The GCD profiles of the DRGO//$Ti_3C_2T_X$@PANI-RGO ZIC at current densities of 0.5, 1, 2, 4, and 6 A g^{-1} (abscissa as the specific capacity) are shown in Figure 10a. In the current density range of 0.5−6 A g^{-1}, the specific capacity of this ZIC was as high as 696.81−269.83 mAh g^{-1}. The discharge capacity of the ZIC was close to the charging capacity, indicating its excellent Coulombic efficiency. With an increase in the current density, the charging and discharging platforms of the ZIC were relatively flat and did not change significantly. The small charge−discharge platform difference means lower irreversibility during cycling. Figure 10b shows the GCD curve of the DRGO//$Ti_3C_2T_X$@PANI-RGO ZIC at different current densities (abscissa as time). In the GCD curve at different current densities, the ZIC showed no significant iR drop, and the shape of the curve did not change dramatically. At the same time, the curvature of the GCD curve also confirmed the

https://doi.org/10.1021/acsami.3c11035
ACS Appl. Mater. Interfaces 2023, 15, 48416−48430

Table 1. Comparison of the Specific Capacitance of Various Zinc Ion Capacitors

cathode	anode	electrolyte	specific capacitance (F g^{-1})	current density (A g^{-1})	ref
PDA-MXene	Zn foil	2 M $ZnSO_4$	124.4	0.2	50
N−Ti_3C_2	Zn foil	1 M $ZnSO_4$	247.9	0.1	51
diamond fibers (DFs)	Zn/DFs	1 M $ZnSO_4$	246.1	0.2	52
Zn@Ti_3C_2	Ti_3C_2	1 M $ZnSO_4$-gelation	132	0.5	53
AC	SM-Zn	2 M $ZnSO_4$	353	0.5	54
porous bamboo carbons	Zn foil	1 M $Zn(CF_3SO_3)_2$	321.3	1.0	55
AC	PAM/PVP-Zn	3 M $Zn(CF_3SO_3)_2$	366	0.5	56
EG/PANI	POP-TAPP-NTCA	2 M $ZnSO_4$	172	0.13	57
DRGO	$Ti_3C_2T_X$@PANI-RGO	2 M $ZnSO_4$	848.77	0.5	this work

stability of the device. The GCD curve of the ZIC was nonlinear, which was closely related to the rapid transfer of Zn^{2+} ions in the electrolyte between the positive and negative electrodes during the charge/discharge possess. However, as the current density increased, the ZIC underwent some polarization and the curvature inevitably shifted. In fact, the specific capacitance decreased as the current density increased (Figure 10c). $ZnSO_4$ reacted with OH^- in the aqueous solution during charge−discharge, forming $Zn_4SO_4(OH)_6{\cdot}5H_2O$. The reactions can be expressed as follows, $H_2O \leftrightarrow H^+ + OH^-$; $4Zn^{2+} + 6OH^- + SO4^{2-} + 5H_2O \leftrightarrow Zn_4SO_4(OH)_6{\cdot}5H_2O\downarrow$. After several charge−discharge cycles, $Zn_4SO_4(OH)_6{\cdot}5H_2O$ precipitated on the electrode surface. This weakened the electrochemical reaction dynamics, resulting in a low Coulombic efficiency and rate performance. However, with such a wide potential difference (0−3.0 V), the DRGO//$Ti_3C_2T_X$@PANI-RGO ZIC retained 41.46% more capacitance than 848.77 F g^{-1} at 0.5 A g^{-1} and 41.46% at 6 A g^{-1}, confirming its obvious rate performance and stability.

As shown in Figure 10d, the specific capacitance of the DRGO//$Ti_3C_2T_X$@PANI-RGO ZIC at 0.5, 1, 2, 4, and 6 A g^{-1} was 848.77, 638.82, 609.07, 360.89, and 351.89 F g^{-1}, respectively. Compared to other ZICs, the DRGO//$Ti_3C_2T_X$@PANI-RGO ZIC showed a high specific capacitance (Table 1),[50−57] likely due to the balanced matching of the ZIC capacitance effect and the battery effect. As shown in the Ragon plot (Figure 10e), the $Ti_3C_2T_X$@PANI-RGO//DRGO ZIC exhibited an ultrahigh energy density of 1060.96 Wh kg^{-1} at a power density of 761.32 W kg^{-1} and 439.87 Wh kg^{-1} at 9786.86 W kg^{-1}. Compared to other ZICs, the energy density of the DRGO//$Ti_3C_2T_X$@PANI-RGO ZIC was also very high,[58−65] which confirmed the feasibility of increasing the SC energy density by rational device designs. As shown in Figure 10f, the cycle stability of the DRGO//$Ti_3C_2T_X$@PANI-RGO ZIC device was detected by repeating the GCD measurements 4000 times at 6 A g^{-1}. ZICs retained 67.9% of the initial capacitance, indicating long-lasting stability and a low leakage rate in its cycling. Nevertheless, the cycle stability of ZIC remained nonideal, and in future work, it is necessary to continue to explore other strategies to improve the cycle stability of the device for practical applications.

CONCLUSIONS

In this study, 3D porous hierarchical $Ti_3C_2T_X$@PANI-RGO heterostructure hydrogels were prepared using a simple strategy. PANI conductive polymer nanofibers were deposited onto the surface of the highly conductive $Ti_3C_2T_X$ matrix via a uniform chemical adsorption and polymerization reaction to inhibit dense stacking, and the $Ti_3C_2T_X$@PANI heterostructures were synthesized. Subsequently, by a GO-assisted low-temperature self-convergence hydrothermal strategy, the $Ti_3C_2T_X$@PANI heterostructure was assembled into the porous 3D cross-linked framework of hydrogels, and the $Ti_3C_2T_X$@PANI-RGO heterostructure hydrogels were prepared. The 3D porous-layered $Ti_3C_2T_X$@PANI-RGO heterostructure hydrogels demonstrated a wide electrochemically active surface area, exceptional electrolyte permeation and ion diffusion, and rapid chemical reaction kinetics, hence leading to a specific capacitance of 848.77 F g^{-1} at 0.5 A g^{-1}. Moreover, the patterning processes of the cocatalytic gasification of metal Co particles produced defects in RGO hydrogels via a low-temperature hydrothermal method. As a result, 3D DRGO hydrogels were prepared and they exhibited a high specific capacitance of 223.52 F g^{-1} at 0.5 A g^{-1}, owing to the extensive and uniform distribution of mesopores on the surface. A ZIC device was then constructed using the 3D $Ti_3C_2T_X$@PANI-RGO heterostructure hydrogels and DRGO hydrogels as anodes and cathodes, respectively. This DRGO//$Ti_3C_2T_X$@PANI-RGO ZIC exhibited a wide potential window (0−3.0 V), high specific capacitance (848.77 F g^{-1} at 0.5 A g^{-1}), ultrahigh energy density (1060.96 Wh kg^{-1} at 761.32 W kg^{-1}, 439.87 Wh kg^{-1} at 9786.86 W kg^{-1}), and long-lasting cycle stability (maintenance of 67.9% of the initial capacitance after 4000 cycles at 6 A g^{-1}). This proposed approach for designing and manufacturing MXene-based hydrogels as anodes and DRGO as cathodes demonstrates a creative strategy to attain a high energy density of ZICs.

AUTHOR INFORMATION

Corresponding Authors

Zenghui Qiu − *College of Mathematics & Physics, Beijing University of Chemical Technology, Beijing 100029, China; Beijing Bioprocess Key Laboratory, Beijing University of Chemical Technology, Beijing 100029, China*; Email: zhqiu@buct.edu.cn

Haijun Xu − *College of Mathematics & Physics, Beijing University of Chemical Technology, Beijing 100029, China; Beijing Bioprocess Key Laboratory, Beijing University of Chemical Technology, Beijing 100029, China*; Email: hjxu@buct.edu.cn

Shaowei Chen − *Department of Chemistry and Biochemistry, University of California, Santa Cruz, California 95064, United States*; orcid.org/0000-0002-3668-8551; Email: shaowei@ucsc.edu

Authors

Peng Liao − *College of Mathematics & Physics, Beijing University of Chemical Technology, Beijing 100029, China; Beijing Bioprocess Key Laboratory, Beijing University of Chemical Technology, Beijing 100029, China*

https://doi.org/10.1021/acsami.3c11035
ACS Appl. Mater. Interfaces 2023, 15, 48416−48430

Xin Zhang − *College of Mathematics & Physics, Beijing University of Chemical Technology, Beijing 100029, China; Beijing Bioprocess Key Laboratory, Beijing University of Chemical Technology, Beijing 100029, China*
Wenjie Yan − *College of Mathematics & Physics, Beijing University of Chemical Technology, Beijing 100029, China; Beijing Bioprocess Key Laboratory, Beijing University of Chemical Technology, Beijing 100029, China*
Colton Jones − *Department of Chemistry and Biochemistry, University of California, Santa Cruz, California 95064, United States*

Complete contact information is available at: https://pubs.acs.org/10.1021/acsami.3c11035

Author Contributions

The manuscript was written through contributions of all authors. All authors have given approval to the final version of the manuscript.

Notes

The authors declare no competing financial interest.

■ ACKNOWLEDGMENTS

The authors acknowledge support from the National Key Research and Development Program of China (No. 2022YFC2105900), the National Natural Science Foundation of China (Nos. 52073022 and 31961133017), and the National Basic Research Program of China (No. 52014CB745100).

■ REFERENCES

(1) Lamba, P.; Singh, P.; Singh, P.; Singh, P.; Bharti; Kumar, A.; Gupta, M.; Kumar, Y. Recent Advancements in Supercapacitors Based on Different Electrode Materials: Classifications, Synthesis Methods and Comparative Performance. *J. Energy Storage* **2022**, *48*, No. 103871.
(2) Lokhande, P. E.; Chavan, U. S.; Pandey, A. Materials and Fabrication Methods for Electrochemical Supercapacitors: Overview. *Electrochem Energy Rev.* **2020**, *3*, 155−186.
(3) Jiang, T. T.; Wang, Y. C.; Chen, G. Electrochemistry of Titanium Carbide MXenes in Supercapacitor. *Small Methods* **2023**, *7*, No. 2201724.
(4) Chatterjee, D. P.; Nandi, A. K. A Review on the Recent Advances in Hybrid Supercapacitors. *J. Mater. Chem. A* **2021**, *9*, 15880−15918.
(5) Pershaanaa, M.; Bashir, S.; Ramesh, S.; Ramesh, K. Every bite of Supercap: A Brief Review on Construction and Enhancement of Supercapacitor. *J. Energy Storage* **2022**, *50*, No. 104599.
(6) Jiang, Y.; Liu, J. Definitions of Pseudocapacitive Materials: A Brief Review. *Energy Environ. Mater.* **2019**, *2*, 30−37.
(7) Choi, C.; Ashby, D. S.; Butts, D. M.; DeBlock, R. H.; Wei, Q. L.; Lau, J.; Dunn, B. Achieving High Energy Density and High Power Density with Pseudocapacitive Materials. *Nat. Rev. Mater.* **2020**, *5*, 5−19.
(8) Shah, S. S.; Das, H. T.; Barai, H. R.; Aziz, M. A. Boosting the Electrochemical Performance of Polyaniline by One-step Electrochemical Deposition on Nickel Foam for High-performance Asymmetric Supercapacitor. *Polymers* **2022**, *14*, 270.
(9) Nagamuthu, S.; Zhang, Y. M.; Xu, Y.; Sun, J. F.; Zhang, Y. M.; Zaman, F. U.; Denis, D. K.; Hou, L. R.; Yuan, C. Z. Non-lithium-based Metal Ion Capacitors: Recent Advances and Perspectives. *J. Mater. Chem. A* **2022**, *10*, 357−378.
(10) Yan, J. P.; Ang, E. H.; Yang, Y.; Zhang, Y. F.; Ye, M. H.; Du, W. C.; Li, C. C. High-voltage Zinc-ion Batteries: Design Strategies and Challenges. *Adv. Funct Mater.* **2021**, *31*, No. 2010213.
(11) Yin, J.; Zhang, W. L.; Alhebshi, N. A.; Salah, N.; Alshareef, H. N. Electrochemical Zinc Ion Capacitors: Fundamentals, Materials, and Systems. *Adv. Energy Mater.* **2021**, *11*, No. 2100201.
(12) Jin, J. L.; Geng, X. S.; Chen, Q.; Ren, T. L. A Better Zn-ion Storage Device: Recent Progress for Zn-ion Hybrid Supercapacitors. *Nano-Micro Lett.* **2022**, *14*, 64.
(13) Xu, J. T.; Dou, Y. H.; Wei, Z. X.; Ma, J. M.; Deng, Y. H.; Li, Y. T.; Liu, H. K.; Dou, S. X. Recent Progress in Graphite Intercalation Compounds for Rechargeable Metal (Li, Na, K, Al)-ion Batteries. *Adv. Sci.* **2017**, *4*, No. 1700146.
(14) Ding, J.; Hu, W. B.; Paek, E.; Mitlin, D. Review of Hybrid Ion Capacitors: From Aqueous to Lithium to Sodium. *Chem. Rev.* **2018**, *118*, 6457−6498.
(15) Guo, Y. H.; Bae, J.; Zhao, F.; Yu, G. H. Functional Hydrogels for Next-generation Batteries and Supercapacitors. *Trends Chem.* **2019**, *1*, 335−348.
(16) Yuan, J.; Hu, X.; Liu, Y. J.; Zhong, G. B.; Yu, B.; Wen, Z. H. Recent Progress in Sodium/Potassium Hybrid Capacitors. *Chem. Commun.* **2020**, *56*, 13933−13949.
(17) Liu, M. Q.; Chang, L. M.; Le, Z. Y.; Jiang, J. M.; Li, J. H.; Wang, H. R.; Zhao, C. M.; Xu, T. H.; Nie, P.; Wang, L. M. Emerging Potassium-ion Hybrid Capacitors. *ChemSusChem* **2020**, *13*, 5837−5862.
(18) Li, Z.; An, Y.; Dong, S.; Chen, C.; Wu, L.; Sun, Y.; Zhang, X. Progress on Zinc Ion Hybrid Supercapacitors: Insights and Challenges. *Energy Storage Mater.* **2020**, *31*, 252−266.
(19) Ma, R.; Chen, Z. T.; Zhao, D. N.; Zhang, X. J.; Zhuo, J. T.; Yin, Y. J.; Wang, X. F.; Yang, G. W.; Yi, F. $Ti_3C_2T_X$ MXene for Electrode Materials of Supercapacitors. *J. Mater. Chem. A* **2021**, *9*, 11501−11529.
(20) Panda, S.; Deshmukh, K.; Theerthagiri, J.; Manickam, S.; Pasha, S. K. K.; Choi, M. Y. MXene Based Emerging Materials for Supercapacitor Applications: Recent Advances, Challenges, and Future Perspectives. *Coord. Chem. Rev.* **2022**, *462*, No. 214518, DOI: 10.1016/j.ccr.2022.214518.
(21) Hemanth, N. R.; Kandasubramanian, B. Recent Advances in 2D MXenes for Enhanced Cation Intercalation in Energy Harvesting Applications: A review. *Chem. Eng. J.* **2020**, *392*, No. 123678.
(22) Li, K.; Liang, M.; Wang, H.; Wang, X.; Huang, Y.; Coelho, J.; Pinilla, S.; Zhang, Y.; Qi, F.; Nicolosi, V.; Xu, Y. 3D MXene Architectures for Efficient Energy Storage and Conversion. *Adv. Funct Mater.* **2020**, *30*, No. 2000842, DOI: 10.1002/adfm.202000842.
(23) Wang, L.; Peng, M. K.; Chen, J. R.; Tang, X. N.; Li, L. B.; Hu, T.; Yuan, K.; Chen, Y. W. High Energy and Power Zinc Ion Capacitors: A Dual-ion Adsorption and Reversible Chemical Adsorption Coupling Mechanism. *ACS Nano* **2022**, *16*, 2877−2888.
(24) Liang, C.; Meng, Y.; Zhang, Y.; Zhang, H.; Wang, W.; Lu, M.; Wang, G. Insights into the Impact of Interlayer Spacing on MXene-based Electrodes for Supercapacitors: A review. *J. Energy Storage* **2023**, *65*, No. 107341.
(25) Chen, J.; Chen, H.; Chen, M.; Zhou, W.; Tian, Q.; Wong, C.-P. Nacre-inspired Surface-engineered MXene/Nanocellulose Composite Film for High-performance Supercapacitors and Zinc-ion Capacitors. *Chem. Eng. J.* **2022**, *428*, No. 131380.
(26) Xiong, D. B.; Li, X. F.; Bai, Z. M.; Lu, S. G. Recent Advances in Layered $Ti_3C_2T_X$ MXene for Electrochemical Energy Storage. *Small* **2018**, *14*, No. 1703419.
(27) Liu, W. F.; Zheng, Y. F.; Zhang, Z.; Zhang, Y. N.; Wu, Y. H.; Gao, H. X.; Su, J.; Gao, Y. H. Ultrahigh Gravimetric and Volumetric Capacitance in $Ti_3C_2T_X$ MXene Negative Electrode Enabled by Surface Modification and In-situ Intercalation. *J. Power Sources* **2022**, *521*, No. 230965.
(28) Wang, G. W.; Guan, Y. C.; Wang, Y.; Ding, Y.; Yang, L. Recent Progress in Research and Application of Nano-manipulation Technologies. *Chin. J. Lasers* **2021**, *48*, No. 0802018.
(29) Beygisangchin, M.; Abdul Rashid, S.; Shafie, S.; Sadrolhosseini, A. R.; Lim, H. N. Preparations, Properties, and Applications of Polyaniline and Polyaniline Thin Films-a Review. *Polymers* **2021**, *13*, 2003 DOI: 10.3390/polym13122003.
(30) Eftekhari, A.; Li, L.; Yang, Y. Polyaniline Supercapacitors. *J. Power Sources* **2017**, *347*, 86−107.
(31) Ahirrao, D. J.; Pal, A. K.; Singh, V.; Jha, N. Nanostructured Porous Polyaniline (PANI) Coated Carbon Cloth (CC) as Electrodes

for Flexible Supercapacitor Device. *J. Mater. Sci. Technol.* **2021**, *88*, 168−182.
(32) Boota, M.; Gogotsi, Y. MXene-conducting Polymer Asymmetric Pseudocapacitors. *Adv. Energy Mater.* **2019**, *9*, No. 1802917.
(33) Korkmaz, S.; Kariper, I. A. Graphene and Graphene Oxide Based Aerogels: Synthesis, Characteristics and Supercapacitor Applications. *J. Energy Storage* **2020**, *27*, No. 101038.
(34) Tarcan, R.; Todor-Boer, O.; Petrovai, I.; Leordean, C.; Astilean, S.; Botiz, I. Reduced Graphene Oxide Today. *J. Mater. Chem. C* **2020**, *8*, 1198−1224.
(35) Gao, F.; Zhang, S. R.; Lv, Q. Y.; Yu, B. Recent Advances in Graphene Oxide Catalyzed Organic Transformations. *Chin. Chem. Lett.* **2022**, *33* (5), 2354−2362.
(36) Wei, S. H.; Ma, J. L.; Wu, D. L.; Chen, B.; Du, C. Y.; Liang, L. R.; Huang, Y.; Li, Z. Y.; Rao, F.; Chen, G. M.; Liu, Z. X. Constructing Flexible Film Electrode with Porous Layered Structure by MXene/SWCNTs/PANI Ternary Composite for Efficient Low-grade Thermal Energy Harvest. *Adv. Funct Mater.* **2023**, *33*, No. 2209806.
(37) Konarov, A.; Voronina, N.; Jo, J. H.; Bakenov, Z.; Sun, Y.-K.; Myung, S.-T. Present and Future Perspective on Electrode Materials for Rechargeable Zinc-ion Batteries. *ACS Energy Lett.* **2018**, *3*, 2620−2640.
(38) Tamang, S.; Rai, S.; Bhujel, R.; Bhattacharyya, N. K.; Swain, B. P.; Biswas, J. A Concise Review on GO, rGO and Metal Oxide/rGO Composites: Fabrication and Their Supercapacitor and Catalytic Applications. *J. Alloys Compd.* **2023**, *947*, No. 169588.
(39) Dideikin, A. T.; Vul, A. Y. Graphene Oxide and Derivatives: The Place in Graphene Family. *Front. Phys.* **2019**, *6*, No. 149.
(40) Yu, W.; Li, S. S.; Yang, H. Y.; Luo, J. Progress in the Functional Modification of Graphene/Graphene Oxide: A Review. *Rsc Adv.* **2020**, *10*, 15328−15345.
(41) Zhao, Z. Y.; Bai, P. K.; Du, W. B.; Liu, B.; Pan, D.; Das, R.; Liu, C. T.; Guo, Z. H. An Overview of Graphene and Its Derivatives Reinforced Metal Matrix Composites: Preparation, Properties and Applications. *Carbon* **2020**, *170*, 302−326.
(42) Tang, C.; Zhang, Q. Nanocarbon for Oxygen Reduction Electrocatalysis: Dopants, Edges, and Defects. *Adv. Mater.* **2017**, *29*, No. 1604103.
(43) Yazyev, O. V.; Louie, S. G. Topological Defects in Graphene: Dislocations and Grain Boundaries. *Phys. Rev. B* **2010**, *81*, No. 195420.
(44) Luo, X. Y.; Zheng, H.; Lai, W. D.; Yuan, P.; Li, S. W.; Li, D.; Chen, Y. Defect Engineering of Carbons for Energy Conversion and Storage Applications. *Energy Environ. Mater.* **2023**, *6*, No. e12402.
(45) Zhang, Y. Q.; Tao, L.; Xie, C.; Wang, D. D.; Zou, Y. Q.; Chen, R.; Wang, Y. Y.; Jia, C. K.; Wang, S. Y. Defect Engineering on Electrode Materials for Rechargeable Batteries. *Adv. Mater.* **2020**, *32*, No. 1905923.
(46) Tang, H.; Yao, J. J.; Zhu, Y. R. Recent Developments and Future Prospects for Zinc-ion Hybrid Capacitors: A Review. *Adv. Energy Mater.* **2021**, *11*, No. 2003994.
(47) Yin, J.; Zhang, W. L.; Wang, W. X.; Alhebshi, N. A.; Salah, N.; Alshareef, H. N. Electrochemical Zinc Ion Capacitors Enhanced by Redox Reactions of Porous Carbon Cathodes. *Adv. Energy Mater.* **2020**, *10*, No. 2001705.
(48) Han, Z. Y.; Xiao, X.; Qu, H. J.; Hu, M. L.; Au, C.; Nashalian, A.; Xiao, X.; Wang, Y. X.; Yang, L.; Jia, F. C.; Wang, T. M.; Ye, Z.; Servati, P.; Huang, L. J.; Zhu, Z. J.; Tang, J. G.; Chen, J. Ultrafast and Selective Nanofiltration Enabled by Graphene Oxide Membranes with Unzipped Carbon Nanotube Networks. *Acs Appl. Mater. Interfaces* **2022**, *14*, 1850−1860.
(49) Liao, P.; Zeng, Y.; Qiu, Z.; Hao, S.; He, J.; Xu, H.; Chen, S. 3D $Ti_3C_2T_X$@PANI-Reduced Graphene Oxide Hydrogel and Defective Reduced Graphene Oxide Hydrogel as Anode and Cathode for High-energy Asymmetric Supercapacitor. *J. Alloys Compd.* **2023**, *948*, No. 169593, DOI: 10.1016/j.jallcom.2023.169593.
(50) Peng, M. K.; Wang, L.; Li, L. B.; Tang, X. N.; Huang, B. Y.; Hu, T.; Yuan, K.; Chen, Y. W. Manipulating the Interlayer Spacing of 3D MXenes with Improved Stability and Zinc-ion Storage Capability. *Adv. Funct Mater.* **2022**, *32*, No. 2109524.
(51) Jin, Y.; Ao, H.; Qi, K.; Zhang, X.; Liu, M.; Zhou, T.; Wang, S.; Xia, G.; Zhu, Y. A High-rate, Long Life, and Anti-self-discharge Aqueous N-doped Ti_3C_2/Zn Hybrid Capacitor. *Mater. Today Energy* **2021**, *19*, No. 100598.
(52) Jian, Z.; Yang, N. J.; Vogel, M.; Leith, S.; Schulte, A.; Schonherr, H.; Jiao, T. P.; Zhang, W. J.; Muller, J.; Butz, B.; Jiang, X. Flexible Diamond Fibers for High-energy-density Zinc-ion Supercapacitors. *Adv. Energy Mater.* **2020**, *10*, No. 2002202.
(53) Yang, Q.; Huang, Z. D.; Li, X. L.; Liu, Z. X.; Li, H. F.; Liang, G. J.; Wang, D. H.; Huang, Q.; Zhang, S. J.; Chen, S. M.; Zhi, C. Y. A Wholly Degradable, Rechargeable Zn-Ti_3C_2 MXene Capacitor with Superior Anti-self-discharge Function. *ACS Nano* **2019**, *13*, 8275−8283.
(54) An, G.-H.; Cha, S.; Sohn, J. I. Surface Tailoring of Zinc Electrodes for Energy Storage Devices with High-energy Densities and Long Cycle Life. *Appl. Surf. Sci.* **2019**, *467*−*468*, 1157−1160.
(55) Wang, J.; Huang, Y.; Han, X.; Li, Z.; Zhang, S.; Zong, M. A Flexible Zinc-ion Hybrid Supercapacitor Constructed by Porous Carbon with Controllable Structure. *Appl. Surf. Sci.* **2022**, *579*, No. 152247.
(56) Li, Z. G.; Deng, W. J.; Li, C.; Wang, W. J.; Zhou, Z. Q.; Li, Y. B.; Yuan, X. R.; Hu, J.; Zhang, M.; Zhu, J. L.; Tang, W.; Wang, X.; Li, R. Uniformizing the Electric Field Distribution and Ion Migration During Zinc Plating/Stripping Via a Binary Polymer Blend Artificial Interphase. *J. Mater. Chem. A* **2020**, *8*, 17725−17731.
(57) Jing, W. J.; Cui, X. K.; Kong, F. B.; Wei, W.; Li, Y. C.; Fan, L. Z.; Li, X. H. Fe-N/C Single-atom Nanozyme-based Colorimetric Sensor Array for Discriminating Multiple Biological Antioxidants. *Analyst* **2021**, *146*, 207−212.
(58) Lou, G.; Pei, G.; Wu, Y.; Lu, Y.; Wu, Y.; Zhu, X.; Pang, Y.; Shen, Z.; Wu, Q.; Fu, S.; Chen, H. Combustion Conversion of Wood to N, O Co-doped 2D Carbon Nanosheets for Zinc-ion Hybrid Supercapacitors. *Chem. Eng. J.* **2021**, *413*, No. 127502.
(59) Lu, Y.; Li, Z.; Bai, Z.; Mi, H.; Ji, C.; Pang, H.; Yu, C.; Qiu, J. High Energy-power Zn-ion Hybrid Supercapacitors Enabled by Layered B/N Co-doped Carbon Cathode. *Nano Energy* **2019**, *66*, No. 104132.
(60) Chen, S. M.; Ma, L. T.; Zhang, K.; Kamruzzaman, M.; Zhi, C. Y.; Zapien, J. A. A flexible Solid-state Zinc Ion Hybrid Supercapacitor Based on Co-polymer Derived Hollow Carbon Spheres. *J. Mater. Chem. A* **2019**, *7*, 7784−7790.
(61) Wang, S.; Wang, Q.; Zeng, W.; Wang, M.; Ruan, L.; Ma, Y. A New Free-standing Aqueous Zinc-ion Capacitor Based on MnO_2−CNTs Cathode and MXene Anode. *Nano-Micro Lett.* **2019**, *11*, No. 70, DOI: 10.1007/s40820-019-0301-1.
(62) Wang, Y.; Cao, J.; Guo, J. H.; Zhang, J. L.; Liu, G. S.; Wang, D.; Si, W. M.; Song, J.; Meng, X. X.; Wen, G. W. Flexible Reduced Graphene Oxide/V_2O_5 Composite Battery-type Cathode and MXene Capacitor-type Anode for Aqueous Zinc Ion Hybrid Supercapacitors with High Energy Density. *J. Alloys Compd.* **2022**, *915*, No. 165418.
(63) Li, H. X.; Wu, J.; Wang, L. T.; Liao, Q. X.; Niu, X. H.; Zhang, D. Y.; Wang, K. J. A Zinc Ion Hybrid Capacitor Based on Sharpened Pencil-like Hierarchically Porous Carbon Derived from Metal-organic Framework. *Chem. Eng. J.* **2022**, *428*, No. 131071.
(64) Shi, J.; Wang, S.; Wang, Q.; Chen, X.; Du, X.; Wang, M.; Zhao, Y.; Dong, C.; Ruan, L.; Zeng, W. A New Flexible Zinc-ion Capacitor Based on Delta-MnO_2@Carbon Cloth Battery-type Cathode and MXene@Cotton Cloth Capacitor-type Anode. *J. Power Sources* **2020**, *446*, No. 227345.
(65) Leng, C.; Fedoseeva, Y. V.; Zhao, Z.; Yan, B.; Okotrub, A. V.; Wang, X.; Fan, J.; Qiu, J. Rational-design Heteroatom-doped Cathode and Ion Modulation Layer Modified Zn Anode for Ultrafast Zinc-ion Hybrid Capacitors with Simultaneous High Power and Energy Densities. *J. Power Sources* **2022**, *536*, No. 231484.